

Rapid nonlinear convex guidance using a monomial method

Ethan R. Burnett* and Francesco Topputo†

This paper introduces a framework by which the nonlinear trajectory optimization problem is posed as a path-planning problem in a space liberated of dynamics. In this space, general state constraints for continuous and impulsive control problems are encoded as linear constraints on the native overparameterized variables. This framework is enabled by nonlinear expansion in the vicinity of a reference in terms of fundamental solutions and a minimal nonlinear basis of mixed monomials in problem initial conditions. The former can be computed using state transition tensors, differential algebra, or analytic approaches, and the latter is computed analytically. Nonlinear guidance schemes are proposed taking advantage of this framework, including a successive convex programming scheme for delta-V minimizing trajectory optimization. This work enables a stable, easy to implement, and highly rapid nonlinear guidance implementation without the need for collocation or real-time integration.

1 Introduction

In the context of modern guidance, navigation, and control (GNC), spacecraft autonomy presents itself as a particularly technically and politically challenging problem. Strict computational and hardware limitations are imposed by the need for radiation-hardened processors and on-board power and mass constraints. Experimentation with autonomous agents is furthermore extremely regulated in comparison to terrestrial ventures in autonomy (such as self-driving cars) due to the high risk of testing autonomous capabilities with no flight heritage on extremely expensive space vehicles. In practice, this has always motivated onboard guidance implementations that are computationally lean, deterministic, and easy to test and validate. Nonetheless recent trends in dropping cost-to-orbit and the proliferation of CubeSats anticipate the deployment of numerous lower-cost deep space spacecraft which will require an increased degree of autonomy to avoid overwhelming human-in-the-loop on-ground tracking and planning capabilities (Di Domenico et al., 2023). Thus it seems likely that there will be increasing demand for on-board guidance, including for use in critical planning and decision-making operations, in the years to come. Such “computational guidance and control” schemes (Lu, 2017), making use of greater embedded computation capability, will go far beyond the traditional algebraic operations needed for evaluating closed-form guidance, while retaining the flexibility and trust necessary for onboard use.

The main characteristics of suitable on-board spacecraft guidance, are, according to Starek et al. (2016), that 1) it should be computationally reasonable, 2) it should compute an optimal solution wherever possible, and 3) it should enable verifiability. Convex optimization-based guidance presents an appealing candidate for meeting these challenges of onboard guidance because by nature it is fast, extremely stable, computationally well-posed, and thus easy to profile computationally (Boyd and Vandenberghe, 2004). Within the convex optimization framework, it is also possible to develop *stochastic guidance* schemes that robustly accommodate expected dispersions in control performance as well as state and parameter estimation errors. Chance-constrained methods are becoming popular for this because they provide performance guarantees with a user-defined confidence level – see e.g. Oguri and McMahan (2021) and Berning Jr. et al. (2023). In addition to stochasticity, nonlinearity poses a perennial and ubiquitous challenge. Even for otherwise convex problems, the general non-convexity of nonlinear dynamics often forces an iterative approach via successive

*Marie Skłodowska-Curie Postdoctoral Fellow, Department of Aerospace Science and Technology, Politecnico di Milano, 20156 Milan, Italy ethanryan.burnett@polimi.it

†Professor, Department of Aerospace Science and Technology, Politecnico di Milano, 20156 Milan, Italy

convexification (Mao et al., 2017), whereby a non-convex problem is solved locally as a convex sub-problem subject to trust region constraints to enforce a stable iterative march towards the optimal solution. While extremely powerful, successive convexification implementations tend to require fairly problem-specific details of choice of transcription and trust-region updates to ensure stability, feasibility, and computational efficiency.

Among the aforementioned challenges of on-board guidance, for this work we are focused on methods for fast, robust, and easily characterizable onboard guidance for nonlinear systems. Guidance of nonlinear systems invariably comes with some non-trivial computational cost. However, not all of this cost needs to be paid in real-time, and much can be shifted to non-critical times. This is done by enabling pre-computation of useful and reusable information to the maximum extent possible. Along these motivational lines, we introduce a new framework for using nonlinear expansions of problem dynamics that is demonstrably computationally efficient. It requires no real-time integration, either explicitly (as in predictor-corrector methods or multiple shooting) or implicitly (as with collocation schemes). The method requires in real-time only fairly simple computation and manipulation of matrices and vectors of monomials and standard linear algebra. Furthermore it enables geometrically intuitive and easy-to-implement differential correction and successive convexification schemes for trajectory optimization. The truncated nonlinear expansion of the solution, written in a special ordered quasi-linear form, is our “transcription” scheme. The optimization problem is posed in an efficient manner making use of a special set of coordinates: an overparameterized set of monomials in the osculating “initial conditions” of the problem. The accuracy of the guidance scheme is then easily characterized by ensuring that the problem, when parameterized in these coordinates, always remains within a region of desired accuracy of the domain of the truncated nonlinear expansions.

Many past works are relevant to the ideas and techniques expounded in this work. First, to facilitate our computations, we make use of a computerized monomial algebra, whereby monomial series of an arbitrary order and number of variables are represented by arrays of their coefficients, whose spatial arrangement matches the ordering of the monomial terms. Similar schemes have been implemented before, and Giorgilli and Sansottera (2011) gives a broad overview of commonly used methods. Jorba (1999) develops a computer algebra system in which monomials are computed, stored, and manipulated in a manner very similar to ours. Their applications are otherwise quite different, leveraging manipulation of monomials in a sequence of canonical transformations for the purpose of constructing normal forms and obtaining approximate integrals of Hamiltonian systems.

The other half of our methodology involves the computation of nonlinear fundamental solution expansions about a reference – each associated with a particular unique monomial in the initial conditions. We’ve explored their computation by many means. Firstly, via “State Transition Tensors”, which are an extension of the ubiquitous state transition matrix involved in almost any method involving both linearization and discretization. Park and Scheeres (2006) provide a classic overview, and Boone and McMahon (2021) provide a more recent predictor-corrector guidance implementation for two-burn maneuvers. We have also computed the nonlinear fundamental solutions leveraging Differential Algebra methods, which facilitates automated computation of derivatives via a structure allowing direct treatment of many topics related to the differentiation and integration of functions (Berz, 1999). This methodology has seen noteworthy use in spaceflight GNC in uncertainty propagation (Valli et al., 2013) and optimal control (Di Lizia et al., 2014; Greco et al., 2020). Lastly, nonlinear fundamental solution expansions can be computed analytically for some specialized problems. This is typically aided nowadays by the use of computational software such as Mathematica (Wolfram Research, Inc., 2023), and usually involves the use of perturbation methods (Nayfeh, 2000; Hinch, 1991). In this work, our example application is one for which many such expansions have been analytically derived: the spacecraft relative motion and rendezvous problem. References such as Butcher et al. (2016), Butcher et al. (2017), Willis et al. (2019b), and Willis et al. (2019a) are thus especially relevant to us.

This work makes use of convex optimization for trajectory optimization. In addition to the thorough foundational work of Boyd and Vandenberghe (2004), see also work outlining the successive convexification algorithm SCvx (Mao et al., 2017) and recent improvements (e.g. Oguri (2023) for an augmented Lagrangian formulation to enable a feasibility guarantee of SCvx). Python is our chosen language for convex optimization prototyping, offering mature open-source tools such as CVXPY (Diamond and Boyd, 2016; Agrawal et al., 2018) and ECOS (Domahidi et al., 2013), as well as the recent introduction of CVXPYgen (Schaller et al.,

2022) for especially rapid problem-solving via generation of a speedy custom solver implementation in C called directly from the Python implementation as a CVXPY solver method. For a clear and simple introduction to convex optimization methods for spacecraft trajectory optimization, see Wang and Grant (2018), and for a discussion of the typically necessary collocation schemes, we recommend Kelly (2017). Our work follows some notable other works making use of convex optimization for trajectory optimization. Much of this work falls under the ERC-funded EXTREMA project (Di Domenico et al., 2023) for self-driving interplanetary CubeSats. Hofmann and Toppito (2021) present a computationally simple and robust convex optimization-based algorithm for low-thrust interplanetary trajectories. Morelli et al. (2022) apply convex optimization to a similar problem while considering a homotopic energy-to-fuel optimal approach along with “second-order” trust region methods. Hofmann et al. (2023) perform a wide study of different discretization and trust region methods for convex low-thrust trajectory optimization. In this early work we lay the groundwork for both continuous and impulsive control, but we explore only the latter in-depth. Our example application is convex optimization of the long-range spacecraft rendezvous problem under impulsive thrust. For applications to the close-range problem with convex programming, see e.g. Berning Jr. et al. (2023) (applying drift safety guarantees) or Burnett and Schaub (2022) (for methods applicable to any general periodic orbits).

This paper is organized as follows. In Section 2, we highlight the fundamental ideas behind our methodology. We discuss the ideas of osculating initial conditions and overparameterized monomial representations, which are both central and necessary to this work. In Section 3 we move on to the applications of our framework to spacecraft trajectory optimization, culminating in an example simple successive convexification implementation whose real-time operations are computationally extremely lean and easy to implement. In Section 4 we provide a thorough example application to the nonlinear spacecraft rendezvous problem. Section 4.1 provides a simple two-stage (linear prediction, nonlinear correction) convex guidance strategy leveraging our developments. Finally, Section 4.2 showcases illustrates the successive convexification scheme from Section 3, and in Sections 4.3 and 4.4 the principles explained in this paper are used to develop more complex examples. We make concluding remarks and suggestions for future work in Section 5.

2 Theory

2.1 Osculating Initial Conditions

This work considers controlled dynamical systems with dynamics of the following control-affine form:

$$\dot{\mathbf{x}} = \mathbf{f}(\mathbf{x}, t) + B(\mathbf{x}, t)\mathbf{u} \quad (1)$$

where $\mathbf{u} \in \mathbb{R}^m$ is a control signal, $\mathbf{x} \in \mathbb{R}^N$ is a state deviation, and t is time. This form also admits the simpler cases where $B(\mathbf{x}, t)$ is not a function of the state, or is constant altogether. In general, our methodology is nonlinear but still *local* – we consider the controlled motion of a state deviation $\mathbf{x}(t)$ in the vicinity of a natural or controlled reference trajectory $\mathbf{X}_r(t)$, or similarly, an equilibrium point \mathbf{X}_r^* . To avoid burdensome notation, we never show the δ on such state deviations from a reference, and hereafter we use $\mathbf{X}_r(t)$ when needed to refer to any reference, with $X_{r,i}$ for the i^{th} component of the reference state vector, and lowercase $\mathbf{x}(t)$ for any departure, with x_i for the i^{th} component of the state deviation. Thus always “ $\delta\mathbf{x}$ ” $\equiv \mathbf{x}$, whereby the origin $\mathbf{x} = \mathbf{0}$ denotes a point of zero departure from some reference/equilibrium point.

For any valid initial condition of a deviation (henceforth simply a “state”) $\mathbf{x}(0)$ and a time $t > 0$, we can get the state $\mathbf{x}(t)$ by application of the *flow of the natural dynamics* (i.e., control-free, $\mathbf{u} = \mathbf{0}$) as $\mathbf{x}(t) = \varphi(\mathbf{x}(0), t, 0)$ and similarly the inverse mapping obtains the initial conditions implied by the state at time t from the flow of the natural dynamics:

$$\mathbf{x}(0) = \varphi^{-1}(\mathbf{x}(t), t, 0) \quad (2)$$

where e.g. $\varphi(\mathbf{x}, t_2, t_1)$ propagates a state $\mathbf{x} \in \mathbb{R}^N$, without control, from t_1 to t_2 . Based on Eq. (2), we could also take some controlled state $\mathbf{x}(t)$ at some time $t > 0$ and back-propagate to a corresponding fictitious or “osculating” initial condition at time 0. We denote this osculating initial condition as $\mathbf{c}_1(t)$. This is depicted in Figure 1. As the trajectory evolves, the osculating initial condition will assume different values over time. Consider that $\mathbf{c}_1(0) = \mathbf{x}(0)$, but at time $0 + \delta t$, the osculating initial condition will have moved a bit if

any control was applied in the interval $[0, \delta t]$. By a general time t , it will have moved smoothly under the action of smooth control to the depicted location, or impulsively, via jump(s), under the action of impulsive control. The mapping to and from $\mathbf{x}(t)$ is always well-defined for our problems of interest, so the \mathbf{c}_1 serves as an equally valid coordinate description of the problem. In this sense, for a controlled state $\mathbf{x}(t)$, there is always an “osculating” fictitious initial state $\mathbf{c}_1(t)$:

$$\mathbf{c}_1(t) = \varphi^{-1}(\mathbf{x}_c(t), t, 0) \quad (3)$$

where the subscript “c” emphasizes that the state $\mathbf{x}(t)$ may be subject to some kind of control. Conveniently, this osculating state is stationary whenever control is not being applied, thus this parameterization removes the influence of natural dynamics.

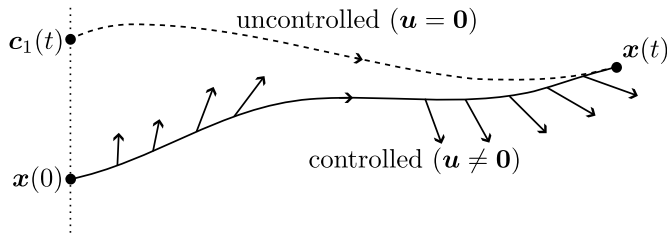


Figure 1: Osculating Initial Conditions

For a linear dynamical system, the transformation φ is linear and easy to compute, and so past works have explored solving linearized guidance problems leveraging parameterization in terms of the osculating initial conditions (or more generally, integration constants) of the system (Guffanti and D’Amico, 2018; Burnett and Schaub, 2022). This transcribes trajectory optimization problems as path planning problems in a transformed domain where the state $\mathbf{c}_1(t)$ moves only via control, with otherwise null dynamics. For nonlinear systems, by contrast, we are accustomed to computing the mapping φ or its inverse via relatively costly numerical integration techniques. Because of this, a general reformulation of nonlinear guidance or control problem in terms of initial states previously would not be considered much of an improvement on the problem to be solved (and indeed, would seem unnecessarily complex). In this work we develop a practical method valid for nonlinear systems in the vicinity of some reference.

2.2 Overparameterized Representation

Instead of a minimal parameterization (linear in the initial conditions), a complex but critical development is to instead consider the parameterization our system by \mathbf{c}_j – a collection of all unique mixed monomials up to j^{th} order, generated from the N initial states $x_1(0), \dots, x_N(0)$. Thus the aforementioned \mathbf{c}_1 is just \mathbf{c}_j for $j = 1$. For $j > 1$, $\mathbf{c}_j \subseteq \mathbb{R}^{K_j}$, with K_j given below:

$$K_j = \sum_{q=1}^j \binom{N+q-1}{q} \quad (4)$$

One approach for building an ordered \mathbf{c}_j is as follows. For all unique mixed monomials of a given order r , multiply by $x_1(0)$, and append to the list. Then multiply the order- r mixed monomials by $x_2(0)$, and append in order only the non-repeated values, repeating this procedure through all state variables to $x_N(0)$. This process initializes with $\mathbf{c}_1 = \mathbf{x}(0)$ and $r = 1$, and finishes after $r = j - 1$ to produce \mathbf{c}_j . For example, for $N = 3$, $j = 2$, \mathbf{c}_2 is computed as below:

$$\mathbf{c}_2 = (x_1(0), x_2(0), x_3(0), x_1^2(0), x_1x_2(0), x_1(0)x_3(0), x_2^2(0), x_2(0)x_3(0), x_3^2(0))^{\top} \quad (5)$$

We provide some more discussion of this procedure in Appendix A. See e.g. Giorgilli and Sansottera (2011) and Jorba (1999) for more details about the computerized algebraic manipulation of sets of monomials.

With the construction of \mathbf{c}_j established, we can in general nonlinearly expand the solution of a dynamical system about a fixed point (or an arbitrary reference, w.l.o.g.) in terms of unique monomials and their associated fundamental solutions as below:

$$\begin{aligned} \mathbf{x}(t) &\approx x_1(0)\boldsymbol{\psi}_{x_1}(t) + x_2(0)\boldsymbol{\psi}_{x_2}(t) + \dots + x_N(0)\boldsymbol{\psi}_{x_N}(t) \\ &\quad + x_1^2(0)\boldsymbol{\psi}_{x_1^2}(t) + x_1(0)x_2(0)\boldsymbol{\psi}_{x_1x_2}(t) + \dots + x_N^2(0)\boldsymbol{\psi}_{x_N^2}(t) \\ &\quad + \dots \\ &\quad + x_1^j(0)\boldsymbol{\psi}_{x_1^j}(t) + x_1^{j-1}(0)x_2(0)\boldsymbol{\psi}_{x_1^{j-1}x_2}(t) + \dots + x_N^j(0)\boldsymbol{\psi}_{x_N^j}(t) \\ &= \boldsymbol{\Psi}_j(t)\mathbf{c}_j \end{aligned} \tag{6}$$

where the ellipses include all unique monomial terms not shown explicitly. The $\boldsymbol{\psi}$ functions are the fundamental solutions with which we expand the dynamics in the vicinity of the reference:

$$\boldsymbol{\psi}_{x_{\alpha_1}\dots x_{\alpha_k}}(t) = \frac{\mathcal{R}(\alpha_1\dots\alpha_k)}{k!} \frac{\partial^k \mathbf{X}_r(t)}{\partial X_{r,\alpha_1}(0)\dots\partial X_{r,\alpha_k}(0)}; \quad t \geq 0 \tag{7}$$

where $\mathcal{R}(\alpha_1\dots\alpha_k)$ denotes the number of unique permutations for the list $X_{r,\alpha_1}\dots X_{r,\alpha_k}$. The $\boldsymbol{\psi}$ functions can be constructed to a given desired order by various means, including using the relevant terms from the associated state transition tensors (STTs) for the problem (Park and Scheeres, 2006; Boone and McMahon, 2021) or the higher-order Taylor map (HOTM) from differential algebra (DA) (Berz, 1999; Valli et al., 2013), computed numerically, or perturbation solutions (Nayfeh, 2000; Hinch, 1991) which are computed analytically. These topics are discussed in greater detail the Appendix A. An important thing to note is that, at a given order, our representation is a minimal representation written in a linear form, whereas the STTs are a redundant representation, written in general in summation form. Eq. (6) reduces to the familiar state transition matrix expression $\mathbf{x}(t) = \Phi(t, 0)\mathbf{x}(0)$ when $j = 1$, retaining only the N linear fundamental solutions $\boldsymbol{\psi}_{x_1}(t)$ through $\boldsymbol{\psi}_{x_N}(t)$ in the first row of Eq. (6). For the general case $j > 1$, the matrix $\boldsymbol{\Psi}_j(t)$ is $N \times K_j$. Thus $\boldsymbol{\Psi}_j$ is a wide (no. columns \geq no. rows) matrix that not only trivially reduces to the STM for $j = 1$, it can be thought of as a flattened (and minimal) STT that still retains a simple 2D matrix form. Like the STM, this matrix is a function of time. We sometimes write this as $\boldsymbol{\Psi}_j(t)$, implying a continuous function, but in practice it is available only at discrete times, $\boldsymbol{\Psi}_j(t_i)$, and furthermore we reserve the use of more explicit notation $\boldsymbol{\Psi}_j(t_i, t_0) \equiv \boldsymbol{\Psi}_j(t_i)$ for epoch time t_0 when needed.

Because \mathbf{c}_j is overparameterized, there are $K_j - N$ constraints relating its nonlinear to its N linear elements. For example, applying a change in the linear component of \mathbf{c}_j associated with $x_1(0)$, the higher-order components of \mathbf{c}_j such as $x_1^2(0)$, $x_1(0)x_2(0)$, $x_1(0)x_3(0)$ etc. are forced to take on a certain value, because they are functionally dependent on the linear components. You can convince yourself of this by computing variations of Eq. (5) based on various values of $\mathbf{x}(0) \in \mathbb{R}^N$, and noting the consequence on the higher-order components' values. Thus \mathbf{c}_j is constrained to lie on an N -dimensional surface that we denote as $\mathcal{C}^{(N)}$, which is embedded in a K_j -dimensional space. Figure 2 depicts for a system $\mathbf{x} = (x, \dot{x})^\top$ (i.e. $N = 2$) the surface obtained with a set of monomials up to order 2 - omitting \dot{x}_0^2 and $x_0\dot{x}_0$ from the second-order monomials (reducing K_j from 5 to 3) to enable a simple 3D drawing. Given a point $\mathbf{c}_j \in \mathcal{C}^{(N)}$, any physically admissible infinitesimal variations $d\mathbf{c}_j$ must lie in the tangent space $T_{\mathbf{c}_j}\mathcal{C}^{(N)}$. Critically, this tangent space is easy to compute. Because the sequence of monomials is uniquely defined by the powers of the constituent state components, the Jacobian $\frac{\partial \mathbf{c}_j}{\partial \mathbf{c}_1}$ admits a simple analytic form, and infinitesimal deviations obey the following:

$$d\mathbf{c}_j \in T_{\mathbf{c}_j}\mathcal{C}^{(N)}; \quad d\mathbf{c}_j = \frac{\partial \mathbf{c}_j}{\partial \mathbf{c}_1} d\mathbf{c}_1 \tag{8}$$

Lastly, we denote the following convenient notation for the mapping between linear ($j = 1$) and nonlinear ($j > 1$) monomial sequences:

$$\mathbf{c}_j = \mathbf{E}_j(\mathbf{c}_1) \tag{9a}$$

$$\mathbf{c}_1 = \mathbf{E}_j^{-1}(\mathbf{c}_j) = \begin{bmatrix} I_{N \times N} & 0_{N \times (K_j - N)} \end{bmatrix} \mathbf{c}_j \tag{9b}$$

where \mathbf{E}_j expands \mathbf{c}_1 into its nonlinear representation of order j and conversely \mathbf{E}_j^{-1} extracts just the linear part \mathbf{c}_1 from \mathbf{c}_j .

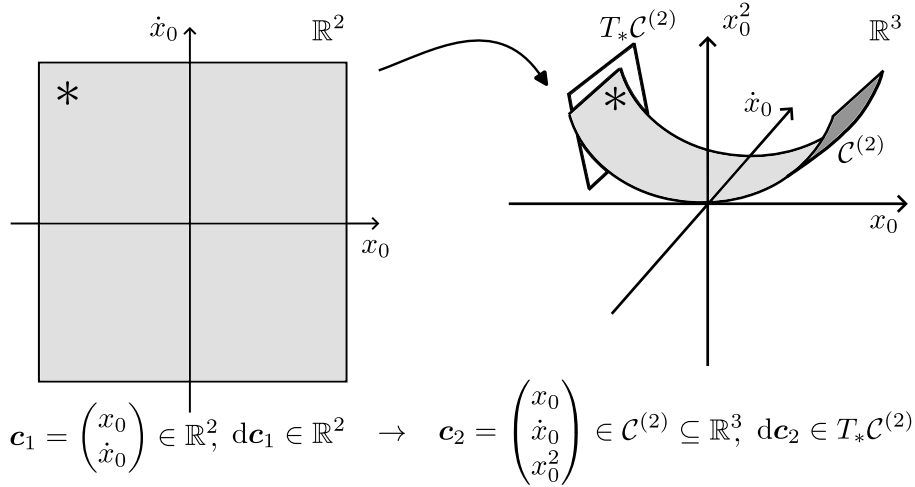


Figure 2: Monomial Coordinates and Initial Conditions

2.3 Kinematics in terms of the monomials

To motivate more complex general arguments, we start with a simplified and specific example. Let $\mathbf{x}(t) = (\mathbf{r}^\top(t), \mathbf{v}^\top(t))^\top$ denote specifically the state in Cartesian coordinates with position $\mathbf{r}(t)$ and velocity $\mathbf{v}(t)$. Thus the state at time t_i obeys the following mapping from the monomial expansion of the initial conditions:

$$\mathbf{x}(t_i) = \Psi_j(t_i)\mathbf{c}_j \quad (10)$$

Eq. (10) is only approximately true for $t_i > 0$, but it becomes more accurate as the order j is increased (consider that the STM will not exactly describe the evolution of the state deviation from $\mathbf{x}(0)$ to $\mathbf{x}(t_i)$, but a second-order expansion will do better within some region of convergence, and third order better still). We defer for now discussion of the error involved in this expression, and limit our arguments to some domain of validity still to be defined.

Let us furthermore limit ourselves for now to the case of control of $\mathbf{x}(t)$ executed via impulsive maneuvers. (This case implies, operationally, that the reference $\mathbf{X}_r(t)$ is a natural trajectory.) For this control problem, we allow for the possibility of a maneuver at any time t_i in a discretized sequence $[t_1, t_2, t_3, \dots, t_K]$. In lieu of considering each $\Delta\mathbf{v}(t_i)$ and the product of their effects across all discretization points, we can instead parameterize the problem in terms of the true initial condition $\mathbf{c}_j(t_0) = \mathbf{E}_j(\mathbf{x}(0))$, the fictitious initial condition $\mathbf{c}_{j,\text{goal}}(t_f)$ which generates $\mathbf{x}_{\text{goal}}(t_f)$ under application of the map $\Psi_j(t_f, t_0)$, and a sequence of intermediate states $\mathbf{c}_j(t_i) = \mathbf{E}_j(\mathbf{c}_1(t_i))$, each of which represents a fictitious initial condition that, under application of the appropriate map $\Psi_j(t_i, t_0)$, intersects with a particular maneuver node at its associated maneuver time t_i . This is illustrated by Figure 3, which depicts the true executed trajectory as a sequence of solid colored lines and the fictitious parts as dashed lines. We show explicitly the action of three maneuvers at times t_1, t_2 , and t_3 , and subsequent maneuvers at discretization times not depicted complete the transition of the system to the goal state. The problem is entirely parameterized in the left-most image: the domain of the osculating initial conditions. Optimization of the trajectory involves a deterministic process of finding the optimal $\mathbf{c}_j(t_i)$ for all t_i . The white regions represent static and evolving domains of validity, still to be discussed.

During an impulsive maneuver applied at some t_i , the position will not change, which provides constraints on admissible jumps in \mathbf{c}_j . Meanwhile, the velocity change is a linear function of the jump in \mathbf{c}_j . These describe kinematic conditions relating the instantaneous state and the overparameterized monomials of the osculating initial conditions, written explicitly below:

$$\Psi_{r,j}(t_i) (\mathbf{c}_j(t_i) - \mathbf{c}_j(t_{i-1})) = \mathbf{0} \quad (11a)$$

$$\Delta\mathbf{v}(t_i) = \Psi_{v,j}(t_i) (\mathbf{c}_j(t_i) - \mathbf{c}_j(t_{i-1})) \quad (11b)$$

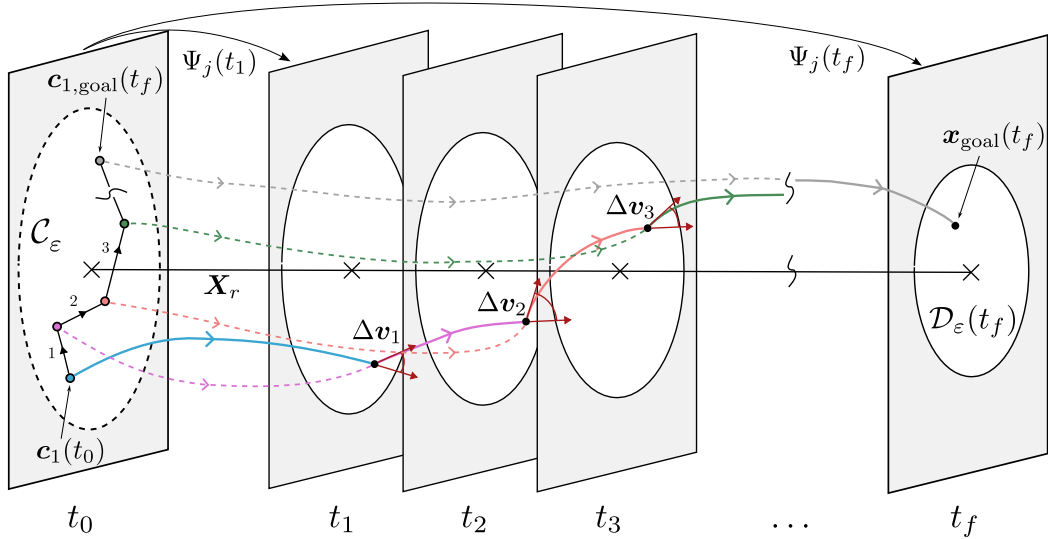


Figure 3: Impulsive maneuver trajectory transcription via Ψ_j

where $\Psi_{r,j}$ denotes the top $N/2$ (position-associated) rows of Ψ_j , and $\Psi_{v,j}$ the bottom $N/2$ (velocity-associated) rows. This enables the complete parameterization of the trajectory in terms of decision variables $\mathbf{c}_j(t_i) \forall t_i \in [t_1, t_2, t_3, \dots, t_f]$, which can be linearly mapped to the instantaneous state $\mathbf{x}(t_i)$. We will show that this parameterization is extremely powerful. Given pre-computation of the map Ψ_j from t_0 to all times of interest, nonlinear guidance problems can be repeatedly solved with very low recurrent computational cost, via reuse of the map Ψ_j and manageable linear algebra. There are strong opportunities for this methodology in operational situations where a reasonable reference trajectory is known.

2.4 Domain of validity

Because we use a truncated nonlinear map Ψ_j to describe the departure of the state from the reference, in reality our methods are limited to a finite region in the vicinity of the reference trajectory. We present some arguments to enable the quantification of this region, but note we do not give a formal proof. First, we assume that the dynamics in the vicinity of the reference are smooth and continuous and admit a locally convergent Taylor series expansion. We define a scalar measure of the truncation error as

$$e_j(\mathbf{c}_1, t_i) = \|\mathbf{x}_{\text{approx}}(t_i) - \mathbf{x}_{\text{true}}(t_i)\| = \|\Psi_j(t_i, 0)\mathbf{E}_j(\mathbf{c}_1(t_i)) - \boldsymbol{\varphi}(\mathbf{c}_1(t_i), t_i, 0)\| \quad (12)$$

The value of $e_j(\mathbf{c}_1, t)$ tends to increase with the scale of \mathbf{c}_1 (fixing t) and with the scale of t (fixing \mathbf{c}_1).

In lieu of ensuring that each temporal discretization point of the trajectory is contained within an instantaneous domain of validity $\mathcal{D}(t_i)$ (a local neighborhood of the reference $\mathbf{X}_r(t_i)$ for which the expansion about the reference is sufficiently valid), we can instead ensure that the osculating initial conditions of the entire problem lie within a *static* domain of validity \mathcal{C}_ε . We do this by setting an error threshold ε as the max desired truncation error at time t_f , and we consider error sampling of a number of control points \mathbf{c}_1 on a domain C_r :

$$C_r = \{\mathbf{c}_1 : \|\mathbf{c}_1\| = r\} \quad (13)$$

Increasing r from zero (for which $e_j(\mathbf{0}, t) \triangleq 0$), we stop at r_{crit} :

$$r_{\text{crit}} \triangleq r : \max_{\|\mathbf{c}_1\|=r} e_j(\mathbf{c}_1, t_f) = \varepsilon, \quad (14)$$

thus the static domain of validity is defined as:

$$\mathcal{C}_\varepsilon \triangleq \{\mathbf{c}_1 : \|\mathbf{c}_1\| \leq r_{\text{crit}}(\varepsilon)\} \quad (15)$$

This argument exploits the fact that $e_j(\mathbf{c}_1, t)$ tends to grow with increasing t . By bounding the error at a final time of interest t_f , the error at prior times $t_i < t_f$ should also be similarly bounded.

In reality, the information provided by Ψ_j for accurately re-parameterizing the whole problem at the initial time could also somehow be captured by smaller maps (i.e. lower j) from each t_i to t_{i+1} . This is because the approximation afforded by $\Psi_j(t, 0)$ worsens as time $t \geq 0$ increases. However, re-parameterizing the problem at the initial time accomplishes two goals: 1) it facilitates a *linear* transcription of the trajectory optimization problem (extremely useful for developing our convex optimization-based schemes) and 2) it greatly simplifies the effort needed to certify (or ensure) the accuracy of the guidance solution, because we need only check (or enforce) that the optimal path lies within the *static* domain of validity, e.g. $\mathbf{c}_1 \in \mathcal{C}_\varepsilon \forall t_i$.

2.5 Generalizations

2.5.1 Continuous theory: variation of parameters

Here, we extend the prior discretized arguments to the case of continuous control operating in continuous time. The controlled dynamics are given by the equations below. Instead of discrete jumps, we seek the *continuously* varying $\mathbf{c}_j(t)$ such that Eq. (10) continually describes the controlled state. Again we note these arguments only hold in circumstances where the truncation error is negligible. Factoring and differentiating Eq. (10):

$$\dot{\mathbf{r}} = \dot{\Psi}_{r,j} \mathbf{c}_j + \Psi_{r,j} \dot{\mathbf{c}}_j \quad (16a)$$

$$\dot{\mathbf{v}} = \dot{\Psi}_{v,j} \mathbf{c}_j + \Psi_{v,j} \dot{\mathbf{c}}_j \quad (16b)$$

The following kinematic identity must be satisfied, noting that by definition of our choice of coordinates \mathbf{x} , the nonlinear fundamental solutions satisfy $\Psi_{v,j}(t) = \dot{\Psi}_{r,j}(t)$:

$$\begin{aligned} \dot{\mathbf{r}} = \mathbf{v} &= \Psi_{v,j} \mathbf{c}_j \\ &= \dot{\Psi}_{r,j} \mathbf{c}_j \end{aligned} \quad (17)$$

From this we obtain the below constraint on admissible directions of $\dot{\mathbf{c}}_j \in T_{\mathbf{c}_j} \mathcal{C}^{(N)}$:

$$\Psi_{r,j} \dot{\mathbf{c}}_j = \mathbf{0} \quad (18)$$

Then, denoting the natural acceleration \mathbf{a} and the control acceleration $\mathbf{a}_c = B_L(\mathbf{x}, t) \mathbf{u}$ where B_L is the lower $N/2$ rows of control matrix B (and furthermore $B_L = I_{3 \times 3}$ in the general 3D Cartesian case), we obtain also the following relationship from Eq. (16) after noting $\mathbf{a} = \dot{\Psi}_{v,j} \mathbf{c}_j$:

$$\mathbf{a}_c = \Psi_{v,j} \dot{\mathbf{c}}_j \quad (19)$$

Comparing Eqs. (18) and (19), to Eq. (11), we recognize these expressions as a continuous control analog of the earlier kinematic constraints.

2.5.2 Functions and coordinate transformations

Consider some general (and possibly nonlinear) scalar function of the state at a particular time, $g(\mathbf{x}, t)$. Let \mathbf{g} be a smooth function of $\mathbf{x}(t_i)$ that admits a Taylor series, thus it can be written as a multivariate polynomial in the components of $\mathbf{x}(t_i)$. Because each component $x_q(t_i)$ for $q = 1 : N$ is itself a multivariate polynomial in the $x_q(0) \forall q$, and because multivariate polynomials are closed under multiplication and addition, the function $g(\mathbf{x}, t)$ can also be approximated (to order j) as a multivariate polynomial in the $x_q(0)$. Thus $g(\mathbf{x}, t)$ can itself be approximated as a *linear function* of \mathbf{c}_j :

$$g(\mathbf{x}(t_i), t_k) \approx \boldsymbol{\gamma}_j^\top(t_k) \mathbf{c}_j(t_i) \quad (20)$$

for vector $\boldsymbol{\gamma}_j$ of length K_j . Similarly, vector functions of the state, $\mathbf{g}(\mathbf{x}, t) \in \mathbb{R}^p$, as collections of p scalar functions, can be related linearly to \mathbf{c}_j :

$$\mathbf{g}(\mathbf{x}(t_i), t_k) \approx \boldsymbol{\Gamma}_j(t_k) \mathbf{c}_j(t_i) \quad (21)$$

for matrix Γ_j of size $p \times K_j$. In this regard, general functions of the discretized state can be approximated by simple linear functions of the overparameterized monomial state.

There are two immediate consequence of the preceding arguments. First, any admissible nonlinear constraint functions on \mathbf{x} that can be rendered linear in \mathbf{c}_j fit within the convex optimization framework for our parameterization \mathbf{c}_j . Second, the Ψ_j and \mathbf{c}_j can be developed for any desired coordinates $\boldsymbol{\eta}$, then related back to our kinematically convenient Cartesian coordinates \mathbf{x} via use of $\mathbf{x} = \mathbf{g}(\boldsymbol{\eta}, t)$. In other words, the kinematic constraints of Eq. (11) generalize to:

$$\Gamma_{r,j}(t_i) \left(\mathbf{c}_j^{(\eta)}(t_i) - \mathbf{c}_j^{(\eta)}(t_{i-1}) \right) = \mathbf{0} \quad (22a)$$

$$\Delta \mathbf{v}(t_i) = \Gamma_{v,j}(t_i) \left(\mathbf{c}_j^{(\eta)}(t_i) - \mathbf{c}_j^{(\eta)}(t_{i-1}) \right) \quad (22b)$$

where the superscript “ (η) ” emphasizes that the fundamental solutions and monomial states are developed specifically in working coordinates $\boldsymbol{\eta}$. We find that the computation of Γ_j is facilitated greatly by use of open-source differential algebra tools such as Pyaudi (Izzo et al., 2022).

3 Application to spacecraft trajectory optimization

Consider again the optimization of nonlinear spacecraft trajectories composed of 1) impulsive maneuvers, and 2) coast arcs between maneuvers. The monomial coordinates are naturally well-suited for posing this trajectory optimization problem efficiently as a path-planning problem. We start with a simple unconstrained delta-V optimal nonlinear control example. The transcription between monomial coordinates $\mathbf{c}_j \in \mathcal{C}^{(N)}$ and the trajectory $\mathbf{x}(t)$ is shown in an example 4-burn solution in Figure 4, which is a simplified complement to Figure 3 emphasizing the non-Euclidean nature of $\mathcal{C}^{(N)}$. Note the monomial state is stationary in the absence of maneuvers and it is constrained to lie on $\mathcal{C}^{(N)}$, but is otherwise unconstrained, with all discretization nodes free to assume their respective locations such that the overall minimizing path is obtained. We explore two

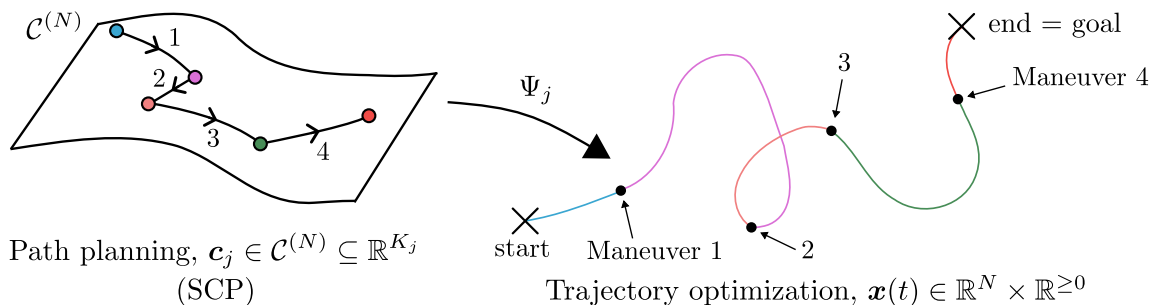


Figure 4: Trajectory Optimization as Path Planning on $\mathcal{C}^{(N)}$, simplified

optimization schemes: minimizing $J = \sum_i \|\Delta \mathbf{v}(t_i)\|^2$ (i.e. “energy-minimizing”) and also $J = \sum_i \|\Delta \mathbf{v}(t_i)\|$ (minimizing delta-V). We differentiate between them by their exponent “ \mathcal{P} ”, 2 or 1. The former is parsed explicitly in this work, whereas the objective function for the latter is implemented via CVXPY parsing.

3.1 Problem formulation

The unconstrained fixed-time optimization problem with impulsive maneuvers is given below:

$$\begin{aligned}
& \text{minimize} && \sum_{i=1}^K \|\Delta \mathbf{v}(t_i)\|^{\mathcal{P}} \\
& \text{subject to} && \begin{aligned} & \mathbf{x}(t_0) = \mathbf{x}_0 \\ & \mathbf{x}(t_K^+) = \mathbf{x}_f \\ & \mathbf{x}(t_{i+1}^-) = \boldsymbol{\varphi}(\mathbf{x}(t_i^+), t_{i+1}, t_i) \\ & \mathbf{r}(t_i^+) = \mathbf{r}(t_i^-) \end{aligned}
\end{aligned} \tag{23}$$

where we explore $\mathcal{P} = 1, 2$, and both yield a convex problem. The trajectory is split into up to $K + 1$ different points, corresponding to an initial condition plus K times where maneuvers are allowed. For $K \gg N$, the optimal solution will generally have $\Delta \mathbf{v}(t_i) = \mathbf{0}$ for many discretized times t_i . The times are not optimization variables; time is discretized a priori. The expression $\boldsymbol{\varphi}(\mathbf{x}(t_1), t_2, t_1)$ denotes the flow of the state $\mathbf{x}(t)$ from t_1 to t_2 , and t_i^- and t_i^+ denote the time t_i at the instants before and after a maneuver $\Delta \mathbf{v}(t_i)$. The first two conditions in Eq. (23) are simple boundary conditions based on prescribed initial and final states of the trajectory. The third condition is a requirement that the state between maneuvers obey the flow of the natural dynamics. The fourth is a continuity condition requiring that the position is unchanged during an instantaneous maneuver.

We seek to rewrite the optimization problem of Eq. (23) in terms of the monomial coordinates. Recall the mapping from monomial coordinates to the instantaneous state at some time t :

$$\mathbf{x}(t) = \Psi_j(t, t_0) \mathbf{c}_j \tag{24}$$

Given an instantaneous maneuver $\Delta \mathbf{v}(t_i)$, the corresponding $\Delta \mathbf{c}_j(t_i) = \mathbf{c}_j(t_i) - \mathbf{c}_j(t_{i-1})$ must satisfy the following for a Ψ_j partitioned row-wise into $\Psi_{r,j}$ (top $N/2$ rows - corresponding to position states) and $\Psi_{v,j}$ (bottom $N/2$ rows - velocity states):

$$\Delta \mathbf{c}_j(t_i) \in \ker(\Psi_{r,j}(t_i, t_0)) \tag{25a}$$

$$\Delta \mathbf{v}(t_i) = \Psi_{v,j}(t_i, t_0) \Delta \mathbf{c}_j(t_i) \tag{25b}$$

$$\mathbf{c}_j(t_{i-1}) + \Delta \mathbf{c}_j(t_i) \in \mathcal{C}^{(N)} \tag{25c}$$

The first constraint is that the position is not changed by the impulsive maneuver. The second constraint is true by definition of the fundamental solution matrix Ψ_j in Cartesian coordinates. The third constraint states that regardless of the change induced in \mathbf{c}_j , the new monomial state must still be on the manifold $\mathcal{C}^{(N)}$. We can now rewrite the problem of Eq. (23):

$$\begin{aligned}
& \text{minimize} && \sum_{i=1}^K \|\Psi_{v,j}(t_i) (\mathbf{c}_j(t_i) - \mathbf{c}_j(t_{i-1}))\|^{\mathcal{P}} \\
& \text{subject to} && \begin{aligned} & \mathbf{c}_j(t_0) = \mathbf{c}_{j,\text{start}} \\ & \mathbf{c}_j(t_K) = \mathbf{c}_{j,\text{goal}} \\ & \mathbf{c}_j(t_i) - \mathbf{c}_j(t_{i-1}) \in \ker(\Psi_{r,j}(t_i)) \\ & \mathbf{c}_j(t_i) \in \mathcal{C}^{(N)}, \quad \forall i \geq 1 \end{aligned}
\end{aligned} \tag{26}$$

The problem is reduced to choosing reasonable discrete steps $\Delta \mathbf{c}_j(t_i)$, $i = 1, 2, \dots, K$, achieving the desired path from $\mathbf{c}_{j,\text{start}}$ at t_0 to $\mathbf{c}_{j,\text{goal}}$ at t_f , while minimizing the above cost. The final state $\mathbf{c}_{j,\text{goal}}$ is obtained from $\mathbf{x}_{\text{goal}}(t_f)$ via a single simple inversion of the map $\Psi_j(t_f, 0)$ (see e.g. Berz (1999)). In particular, the initial guess is given by inversion of the linear part of the map, which is just the STM:

$$\mathbf{c}_{1,\text{goal}}[0] = \Phi^{-1}(t_f, 0) \mathbf{x}_{\text{goal}}(t_f) \tag{27}$$

then subsequent nonlinearity corrections are implemented in a Newton-style framework:

$$\mathbf{c}_{1,\text{goal}}[k] = \mathbf{c}_{1,\text{goal}}[k-1] + \alpha \left(\Psi_j(t_f) \frac{\partial \mathbf{c}_j}{\partial \mathbf{c}_1} \Big|_{\mathbf{c}_{1,\text{goal}}[k-1]} \right)^{-1} (\mathbf{x}_{\text{goal}}(t_f) - \Psi_j(t_f) \mathbf{E}_j(\mathbf{c}_{1,\text{goal}}[k-1])) \quad (28)$$

where k is the iteration number and $\alpha \leq 1$ scales the step for added stability. In our examples the simple choice $\alpha = 1$ was sufficient, and the method was not numerically burdensome, typically executing in Python in ~ 0.01 s for $N = 6$, $j = 3$. Upon convergence, we obtain $\mathbf{c}_{j,\text{goal}} = \mathbf{E}_j(\mathbf{c}_{1,\text{goal}})$.

The problem given by Eq. (26) is intended as a simple example, but in general many functional constraints on the state $\mathbf{x}(t_i)$ can be inherited as linear constraints on the $\mathbf{c}_j(t_i)$. For this optimal path-planning problem, we write out a vector of (preliminary) decision variables as $\tilde{\mathbf{X}} = (\mathbf{c}_j(t_1)^\top, \mathbf{c}_j(t_2)^\top, \dots, \mathbf{c}_j(t_k)^\top)^\top$. The cost function of the problem given by Eq. (26) can be shown to be quadratic in $\tilde{\mathbf{X}}$, and the first two constraints are clearly linear. The third constraint is also linear, written simply as $\Psi_{r,j}(t_i) \Delta \mathbf{c}_j(t_i) = \mathbf{0}$. The only non-convex part of the problem given by Eq. (26) is the final constraint that the decision variables lie on the manifold $\mathcal{C}^{(N)}$. For this non-convexity we propose a successive convex programming problem.

3.2 Successive convex programming

Figure 5 conceptually depicts a trajectory, in terms of 5 distinct points in the monomial coordinates, resulting from 4 impulsive maneuvers. In the vicinity of any of the points in the trajectory shown in

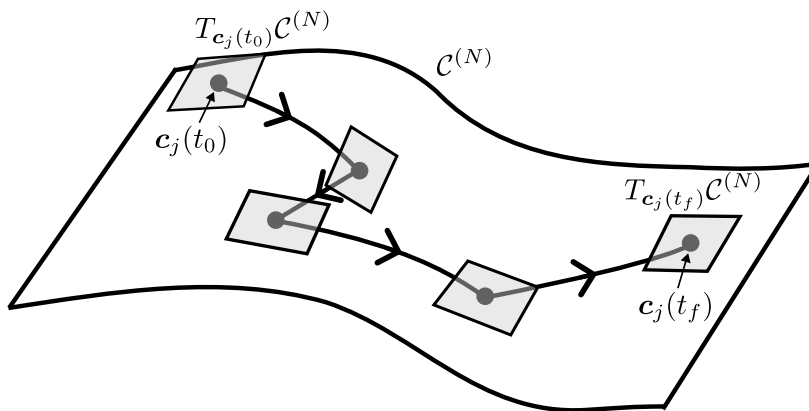


Figure 5: Successive Convexification via Monomial Coordinates on $\mathcal{C}^{(N)}$

Figure 5, we can linearly approximate local variations in \mathbf{c}_j to lie in the tangent space as below:

$$\delta \mathbf{c}_j(t_i) \approx \frac{\partial \mathbf{c}_j}{\partial \mathbf{c}_1} \Big|_{\mathbf{c}_j(t_i)} \delta \mathbf{c}_1(t_i) \in T_{\mathbf{c}_j(t_i)} \mathcal{C}^{(N)} \quad (29)$$

This expression is only true in the infinitesimal sense, but for a sufficiently smooth constraint surface it is a decent approximation for larger variations. In this case we know analytically the form of $\mathcal{C}^{(N)}$, the only non-convexity in our problem. The key to a successive convex programming (SCP) implementation of the problem given by Eq. (26) is to make use of the local tangent plane approximation of Eq. (29), and also to choose our free variables for the convex problem as the $\delta \mathbf{c}_1(t_i)$, with the nominal $\mathbf{c}_j(t_i)$ chosen from a prior iteration (or, for iteration 1, from the initial guess of the trajectory). Thus $\tilde{\mathbf{X}} = (\delta \mathbf{c}_1(t_1)^\top, \delta \mathbf{c}_1(t_2)^\top, \dots, \delta \mathbf{c}_1(t_K)^\top)^\top$,

and transforming Eq. (26), the resulting convex sub-problem is given below:

$$\begin{aligned}
& \text{minimize} && \left\| \Psi_{v,j}(t_1) \left(\mathbf{c}'_j(t_1) + \left. \frac{\partial \mathbf{c}_j}{\partial \mathbf{c}_1} \right|_1 \delta \mathbf{c}_1(t_1) - \mathbf{c}_j(t_0) \right) \right\|^{\mathcal{P}} + w \left(\sum_{i=1}^K \|\mathbf{s}_i\|^2 + \|\mathbf{s}_{\text{end}}\|^2 \right) \\
& && + \sum_{i=2}^K \left\| \Psi_{v,j}(t_i) \left(\mathbf{c}'_j(t_i) + \left. \frac{\partial \mathbf{c}_j}{\partial \mathbf{c}_1} \right|_i \delta \mathbf{c}_1(t_i) - \mathbf{c}'_j(t_{i-1}) - \left. \frac{\partial \mathbf{c}_j}{\partial \mathbf{c}_1} \right|_{i-1} \delta \mathbf{c}_1(t_{i-1}) \right) \right\|^{\mathcal{P}} \\
& && \tag{30} \\
& \text{subject to} && \Psi_j(t_k) \left(\mathbf{c}'_j(t_k) + \left. \frac{\partial \mathbf{c}_j}{\partial \mathbf{c}_1} \right|_K \delta \mathbf{c}_1(t_k) \right) + \mathbf{s}_{\text{end}} = \mathbf{x}_{\text{goal}}(t_k) \\
& && \Psi_{r,j}(t_1) \left(\mathbf{c}'_j(t_1) + \left. \frac{\partial \mathbf{c}_j}{\partial \mathbf{c}_1} \right|_1 \delta \mathbf{c}_1(t_1) - \mathbf{c}_j(t_0) \right) + \mathbf{s}_1 = \mathbf{0} \\
& && \Psi_{r,j}(t_{i+1}) \left(\mathbf{c}'_j(t_{i+1}) - \mathbf{c}'_j(t_i) + \left. \frac{\partial \mathbf{c}_j}{\partial \mathbf{c}_1} \right|_{i+1} \delta \mathbf{c}_1(t_{i+1}) - \left. \frac{\partial \mathbf{c}_j}{\partial \mathbf{c}_1} \right|_i \delta \mathbf{c}_1(t_i) \right) + \mathbf{s}_{i+1} = \mathbf{0}, i = 1:K-1
\end{aligned}$$

Note the careful parsing of expressions involving $\mathbf{c}_j(t_0)$, which is fixed in this example and is not part of the decision variables. The $(\cdot)'$ denotes terms from the solution to the prior iteration, about which the current iteration is expanded. Furthermore $\left. \frac{\partial \mathbf{c}_j}{\partial \mathbf{c}_1} \right|_i$ is a shorthand for $\left. \frac{\partial \mathbf{c}_j}{\partial \mathbf{c}_1} \right|_{\mathbf{c}'_j(t_i)}$. The enumerated slack variables \mathbf{s}_i are introduced to prevent artificial infeasibility of the convex sub-problem, with a scalar weight $w > 0$ to specify the degree of penalization of slack terms (the converged solution must satisfy $\mathbf{s}_i = \mathbf{0}$). These slack variables can be physically interpreted as the positional defect constraints in the trajectory. There is also an additional slack variable \mathbf{s}_{end} related to the satisfaction of the first listed linear constraint, which is a constraint on the end state, and is similarly penalized. For performance reasons, it is best for the problem states to be rendered non-dimensional, or for the last $N/2$ components of \mathbf{s}_{end} to be rescaled to have the same positional “units” as the \mathbf{s}_i slack variables. In this manner an SCP iteration will not be biased to over/under penalize any components \mathbf{s}_{end} in comparison to the other \mathbf{s}_i . In our experience with this formulation, proper numerical scaling of the free variables and constraints is necessary to ensure good performance when using commercial or open-source solvers.

Between iterations, it is necessary to project the solution to the convex sub-problem (which exists in the union of the tangent planes of points $\mathbf{c}'_j(t_i) \forall i$) back onto the manifold. The most obvious (and computationally easiest) way is to compute for each update $+\delta \mathbf{c}_1(t_i)$ the new $\mathbf{c}_j(t_i)$ given by $\mathbf{c}'_j(t_i) + \delta \mathbf{c}_1(t_i)$, e.g. using Eq. (9).

Because the tangent-plane approximations of variations $\delta \mathbf{c}_j$ are only locally valid, we must additionally impose some kind of trust region constraint preventing the sub-problem from obtaining variations $\delta \mathbf{c}_1(t_i)$ that are too large. In this work we impose a norm constraint on $\tilde{\mathbf{X}}$ to do this:

$$\|\tilde{\mathbf{X}}\| \leq d \tag{31}$$

We can set a fixed trust-region radius d , or alternatively we can update this via a proper trust-region update method such as the one outlined in (Hofmann et al., 2022).

The sub-problem defined by Eq. (30) can be resolved for $\mathcal{P} = 2$ in the form below:

$$\begin{aligned}
& \text{minimize} && \mathbf{X}^\top P \mathbf{X} + \mathbf{q}^\top \mathbf{X} \\
& \text{subject to} && A \mathbf{X} = \mathbf{b} \\
& && \|M \mathbf{X}\| \leq d
\end{aligned} \tag{32}$$

For this formulation, we first augment the preliminary decision variables $\tilde{\mathbf{X}}$ with slack variables $\mathbf{S} = (\mathbf{s}_1^\top, \mathbf{s}_2^\top, \dots, \mathbf{s}_K^\top, \mathbf{s}_{\text{end}}^\top)^\top$ to form $\mathbf{X} = (\tilde{\mathbf{X}}^\top, \mathbf{S}^\top)^\top$, which is of length $(\frac{3}{2}K + 1)N$ for assumed even N . Because we only want to constrain $\tilde{\mathbf{X}}$, the form of M is simple:

$$M = \begin{bmatrix} I_{NK \times NK} & 0_{NK \times N(\frac{K}{2}+1)} \end{bmatrix} \tag{33}$$

Because all constraints in Eq. (30) are linear and fairly simple, it is easy to construct A and \mathbf{b} . The form of P and \mathbf{q} however requires some algebra and will be provided.

While it does not influence the convex sub-problem, we must compute the part of the cost J in Eq. (30) that is not a function of the decision variables of a given iteration. This term is in fact the total cost predicted from the prior iteration, so we denote it as J' , reusing our prime notation:

$$J' = \sum_{i=1}^K \mathbf{c}_j^{\prime\top}(t_i) O_i \mathbf{c}'_j(t_i) - 2\mathbf{c}_j^{\prime\top}(t_i) O_i \mathbf{c}'_j(t_{i-1}) + \mathbf{c}_j^{\prime\top}(t_{i-1}) O_i \mathbf{c}'_j(t_{i-1}) \quad (34a)$$

$$O_i = \Psi_{v,j}^{\top}(t_i) \Psi_{v,j}(t_i) \quad (34b)$$

Thus the solution to Eq. (32) provides the minimal admissible $\delta J = \mathbf{X}^{\top} P \mathbf{X} + \mathbf{q}^{\top} \mathbf{X}$ yielding total cost $J^{(q)} \approx J^{(q-1)} + \delta J^{(q)}$ for iteration q . In reality, after iteration q , the nonlinear projection of the linear step yields the true $J^{(q)}$ after a procedure of 1) nonlinearly updating all $\mathbf{c}'_j(t_i)$, 2) setting all $\delta \mathbf{c}_1(t_i) = \mathbf{0}$ in Eq. (30), then 3) using that to compute the true values of all slack variables, which are simply the true defects in the constraint equations after the nonlinear projection. From this info, we can compute the actual increment in cost δJ . We can use the disparity between the predicted (linear) δJ and the actual (nonlinear) value to determine how nonlinear an SCP iteration was, with greater nonlinearity yielding greater disparity. The two quantities are given below:

$$\delta J_{\text{predict}}^{(q)} = \mathbf{X}^{\top} P \mathbf{X} + \mathbf{q}^{\top} \mathbf{X} \quad (35a)$$

$$\delta J_{\text{actual}}^{(q)} = J^{(q)} - J^{(q-1)} \quad (35b)$$

where P , \mathbf{q} are computed using information from iteration $q - 1$.

We now define the matrix P and vector \mathbf{q} by sequential accounting instead of explicitly writing the large matrices. In this manner, they are initialized as zeros with the correct size, and consideration of each successive cost term in Eq. (30) adds a corresponding part to the matrices whose form is to be defined.

$$P = P_0 + \sum \delta P, \quad P_0 = \mathbf{0}_{L \times L} \quad (36a)$$

$$\mathbf{q} = \mathbf{q}_0 + \sum \delta \mathbf{q}, \quad \mathbf{q}_0 = \mathbf{0}_{L \times 1} \quad (36b)$$

$$L = \left(\frac{3}{2}K + 1 \right) N \quad (36c)$$

Starting with P , the first (t_1), second (slack-associated), and third (indexed) cost terms of Eq. (30) produce the following contributions to P :

$$\delta P_1 = \begin{bmatrix} C_1^{\top} O_1 C_1 & \vdots & \mathbf{0}_{N \times (L-N)} \\ \mathbf{0}_{(L-N) \times N} & \vdots & \mathbf{0}_{(L-N) \times (L-N)} \end{bmatrix} \quad (37a)$$

$$C_1 = \left. \frac{\partial \mathbf{c}_j}{\partial \mathbf{c}_1} \right|_{\mathbf{c}'_j(t_1)}, \quad O_1 = \Psi_{v,j}^{\top}(t_1) \Psi_{v,j}(t_1) \quad (37b)$$

$$\delta P_2 = \begin{bmatrix} \mathbf{0}_{NK \times NK} & \vdots & \mathbf{0}_{NK \times L_S} \\ \mathbf{0}_{L_S \times NK} & \vdots & w \mathbf{I}_{L_S \times L_S} \end{bmatrix} \quad (38a)$$

$$L_S = L - KN = N \left(\frac{K}{2} + 1 \right) \quad (38b)$$

$$\delta P_{3,i} = \begin{bmatrix} \mathbf{0}_{A \times A} & \mathbf{0}_{A \times N} & \mathbf{0}_{A \times N} & \mathbf{0}_{A \times B} \\ \mathbf{0}_{N \times A} & C_{i-1}^{\top} O_i C_{i-1} & -C_{i-1}^{\top} O_i C_i & \mathbf{0}_{N \times B} \\ \mathbf{0}_{N \times A} & -C_i^{\top} O_i C_{i-1} & C_i^{\top} O_i C_i & \mathbf{0}_{N \times B} \\ \mathbf{0}_{B \times A} & \mathbf{0}_{B \times N} & \mathbf{0}_{B \times N} & \mathbf{0}_{B \times B} \end{bmatrix} \quad (39a)$$

$$C_i = \left. \frac{\partial \mathbf{c}_j}{\partial \mathbf{c}_1} \right|_{\mathbf{c}'_j(t_i)}, \quad O_i = \Psi_{v,j}^{\top}(t_i) \Psi_{v,j}(t_i) \quad (39b)$$

$$A = N(i - 2), \quad B = L - Ni, \quad i = 2:K \quad (39c)$$

where the $\delta P_{3,i}$ is added for every applicable index i . Now \mathbf{q} is defined similarly for the first (t_1) and third (indexed) cost terms:

$$\delta \mathbf{q}_1 = \left[2 \left(\mathbf{c}'_j(t_1) - \mathbf{c}_j(t_0) \right)^\top O_1 C_1 \begin{array}{c} \vdots \\ \mathbf{0}_{1 \times L-N} \end{array} \right]^\top \quad (40)$$

$$\delta \mathbf{q}_{2,i} = \left[\begin{array}{c} \mathbf{0}_{1 \times A} \\ \vdots \\ -2 \left(\mathbf{c}'_j(t_i) - \mathbf{c}'_j(t_{i-1}) \right)^\top O_i C_{i-1} \end{array} \begin{array}{c} \vdots \\ 2 \left(\mathbf{c}'_j(t_i) - \mathbf{c}'_j(t_{i-1}) \right)^\top O_i C_i \end{array} \begin{array}{c} \vdots \\ \mathbf{0}_{1 \times B} \end{array} \right]^\top, \quad i = 2:K \quad (41)$$

Beyond the nonlinear projection, the only other nonlinear calculations needed for the setup of Eq. (30) between iterations are 1) the analytic re-computation of all $\left. \frac{\partial \mathbf{c}_j}{\partial \mathbf{c}_1} \right|_i$ Jacobians and 2) the computation of any needed norms. This simple implementation liberates the details of dynamics from the problem representation. The converged solution is guaranteed to retain the full accuracy of the j^{th} -order fundamental solution expansion because it serves as our transcription scheme. Furthermore, given a measure of the domain of validity \mathcal{C}_ε , it is straightforward to enforce trust region radii d_i in the sub-problem such that at all times each $\|\mathbf{c}'_1(t_i) + \delta \mathbf{c}_1(t_i)\|$ for each trajectory node never extends outside the domain of validity, ensuring robustness of the guidance scheme.

4 Examples

In this section, we showcase the potential use of the developments in this paper for an example application from space vehicle guidance. We hope to establish both practical and theoretical interest in this overparameterized monomial formulation.

4.1 Nonlinear spacecraft rendezvous in LEO – Two-stage guidance

Before showing results with an SCP implementation, we demonstrate a two-stage guidance scheme (linear predictor, nonlinear corrector) for rapid generation of trajectories that are both fuel-efficient and dynamically feasible. The methods in this paper can be applied in practically any dynamical environment, but we first consider the classical rendezvous equations with a target in a simple circular Earth orbit. Using the framework in this paper, we demonstrate the following convenient two-stage guidance strategy for spacecraft rendezvous:

Stage 1: Compute a low-fidelity solution by solving the linearized problem (i.e. $j = 1$). This can be done using several state-of-the-art convex optimization-based approaches.

Stage 2: Rapid nonlinear correction, to accommodate for nonlinearity effects. This is done by leveraging computation of the high-fidelity fundamental solution matrix $\Psi_j(t)$ and the analytic expression for the monomial vector \mathbf{c}_j at desired order of nonlinearity j .

The nonlinear fundamental solutions data necessary for Stage 2 can be computed in advance and stored on a spacecraft's guidance computer. With this approach, implementation of Stage 2 is reduced to the use of pre-programmed analytic functions, data lookup, and manageable linear algebra. In settings where many trajectories need to be computed and characterized, pre-computation of the nonlinear fundamental solution data is substantially computationally liberating. For weakly nonlinear cases, this scheme extends the reach of linearized guidance solutions for a small delta-V penalty. For more strongly nonlinear cases, it provides a convenient feasible (but sub-optimal) initial guess for the SCP solver.

4.1.1 Stage 1

First, a suitable linearized rendezvous guidance scheme is defined. The nonlinear dynamics under consideration are those of relative motion in the vicinity of a simple circular Keplerian orbit. This problem is parameterized by the nonlinear equations below for LVLH relative position $\mathbf{r} = (x, y, z)^\top$ and velocity

$\mathbf{v} = (\dot{x}, \dot{y}, \dot{z})$ (Schaub and Junkins, 2018):

$$\ddot{x} - 2n\dot{y} - xn^2 - \frac{\mu}{R^2} = -\frac{\mu}{r^3}(R+x) \quad (42a)$$

$$\ddot{y} + 2n\dot{x} - yn^2 = -\frac{\mu}{r^3}y \quad (42b)$$

$$\ddot{z} = -\frac{\mu}{r^3}z \quad (42c)$$

where R is the circular target orbit radius, n is its orbital mean motion, $r = \sqrt{(R+x)^2 + y^2 + z^2}$ is the chaser's instantaneous orbit radius, and velocities are measured with respect to the target-centered LVLH frame. Note for this example that $\mathbf{X}_r(t)$ is the orbital state of the target spacecraft, but the formulation of Eq. (42) describes only the dynamics of the relative states.

In the vicinity of the target spacecraft, the nonlinear Eq. (42) linearizes to the popular Clohessy-Wiltshire (CW) model (Clohessy and Wiltshire, 1960):

$$\ddot{x} = 2n\dot{y} + 3n^2x \quad (43a)$$

$$\ddot{y} = -2n\dot{x} \quad (43b)$$

$$\ddot{z} = -n^2z \quad (43c)$$

We have explored solving this linear problem in two ways. First, reusing a method from Burnett and Schaub (2022) which indirectly solves for the optimal burn times and directions, then linearly solves for the resultant magnitudes along each direction (see also Guffanti and D'Amico (2018) and references therein). Second, using a slightly slower method that is much more clear in the context of this work, which is defined below as the linearized equivalent of the problem given by Eq. (26):

$$\begin{aligned} & \text{minimize} \quad \sum_{i=1}^K \|\Phi_v(t_i) (\mathbf{c}_1(t_i) - \mathbf{c}_1(t_{i-1}))\|^{\mathcal{P}} \\ & \text{subject to} \quad \mathbf{c}_1(t_0) = \mathbf{c}_{1,\text{start}} \\ & \quad \quad \quad \mathbf{c}_1(t_K) = \mathbf{c}_{1,\text{goal}} \\ & \quad \quad \quad \mathbf{c}_j(t_i) - \mathbf{c}_j(t_{i-1}) \in \ker(\Phi_r(t_i)) \end{aligned} \quad (44)$$

where $\Phi_r = \Psi_{r,1}$ and $\Phi_v = \Psi_{v,1}$ denote the top and bottom halves of the state transition matrix solution to the linearized dynamics in Eq. (43), and they can also be thought of as just the $j = 1$ part of the map Ψ_j computed from Eq. (42). This linearized problem is already convex, for which we define the free variable vector $\mathbf{X} = (\mathbf{c}_1^\top(t_1), \mathbf{c}_1^\top(t_2), \dots, \mathbf{c}_1^\top(t_K))^\top$. The solver reveals the optimal discretized burn times t_{b_i} as those for which non-null jumps in the states are computed, $\mathbf{c}_1(t_{b_i}) - \mathbf{c}_1(t_{b_{i-1}}) \neq \mathbf{0}$. By contrast, for all sub-optimal burn times t_q , the solution to Eq. (44) will compute $\mathbf{c}_1(t_q) - \mathbf{c}_1(t_{q-1}) = \mathbf{0}$ to the precision of the convex solver used.

The solution of Stage 1 consists of the following:

1. A sequence of (linear) monomial states $\mathbf{c}_1(\tau_i)$ at $k+1$ times $\tau_i \in \mathcal{T}$.
2. A list of critical times $\mathcal{T} = [t_0, t_{b_1}, t_{b_2}, \dots, t_{b_k}]$, where $\tau_0 = t_0$ is the initial time and $\tau_i = t_{b_i}$ is the i^{th} burn time. With this notation, $\mathbf{c}_1(t_0)$ represents the epoch state before the control action of the first burn at $t_{b_i} \geq t_0$ is taken.
3. A table of k associated nonzero delta-V vectors.

The outputs of any other guidance algorithm based on linearization and the impulsive maneuver assumptions (see e.g. Berning Jr. et al. (2023) for a recent example of linearized guidance incorporating the practical constraint of passive safety) can also be easily put into this form. Note the use of lower-case “k” instead of “K” from Section 3 because in this context each increment of the index is by definition a (nonzero) maneuver, selected from a much larger set of candidate burn times, thus $k \ll K$.

4.1.2 Stage 2

This scheme is a rapid high-fidelity correction to the solution of Stage 1 which preserves the burn times $t_{b_i} \in \mathcal{T}_b$ and controllable maneuver positions $\mathbf{r}(t_{b_i})$, while altering the magnitude and direction of the delta-Vs $\Delta\mathbf{v}(t_{b_i})$. The result is a guidance solution compatible with the dynamics parameterized by a given nonlinear fundamental solution representation $\Psi_j(t)$ and associated overparameterized monomial set \mathbf{c}_j . The solution is trustworthy if the nonlinear fundamental solution parameterization $\Psi_j(t)$ is accurate for the flight environment and domain under consideration.

For this scheme simple Newton-style correction is sufficient. We define a free variable vector \mathbf{X} in terms of the (first-order) monomials $\mathbf{c}_1(t_{b_i})$, and a constraint vector $\mathbf{F}(\mathbf{X})$, which is driven to zero as the satisfactory \mathbf{X}^* is obtained. This function is linear in the higher-order monomial representation $\mathbf{c}_j(t_{b_i})$ and nonlinear in the $\mathbf{c}_1(t_{b_i})$. We demonstrate now the form of \mathbf{X} and $\mathbf{F}(\mathbf{X})$:

$$\mathbf{X} = (\mathbf{c}_1(t_{b_1})^\top, \mathbf{c}_1(t_{b_2})^\top, \mathbf{c}_1(t_{b_3})^\top, \dots, \mathbf{c}_1(t_{b_k})^\top)^\top \quad (45)$$

$$\mathbf{F}(\mathbf{X}) = \begin{pmatrix} \Psi_{r,j}(\tau_2)\mathbf{c}_j(\tau_2) - \mathbf{r}_G(\tau_2) \\ \Psi_{r,j}(\tau_3)\mathbf{c}_j(\tau_3) - \mathbf{r}_G(\tau_3) \\ \vdots \\ \Psi_{r,j}(\tau_k)\mathbf{c}_j(\tau_k) - \mathbf{r}_G(\tau_k) \\ \hline \Psi_{r,j}(\tau_1)\mathbf{c}_j(\tau_1) - \Psi_{r,j}(\tau_1)\mathbf{c}_j(\tau_0) \\ \Psi_{r,j}(\tau_2)(\mathbf{c}_j(\tau_2) - \mathbf{c}_j(\tau_1)) \\ \Psi_{r,j}(\tau_3)(\mathbf{c}_j(\tau_3) - \mathbf{c}_j(\tau_2)) \\ \vdots \\ \Psi_{r,j}(\tau_k)(\mathbf{c}_j(\tau_k) - \mathbf{c}_j(\tau_{k-1})) \\ \hline \Psi_{v,j}(\tau_k)\mathbf{c}_j(\tau_k) - \mathbf{v}_G(\tau_k) \end{pmatrix} \quad (46)$$

where the nonlinear mapping from $\mathbf{c}_1(\tau_i)$ (and hence from \mathbf{X}) to $\mathbf{c}_j(\tau_i)$ is analytic and straightforward – recall the discussion in Section 2.2. The first set of constraints (above the dashed line) are enforcing that all controllable maneuver locations match the corresponding maneuver location from the guidance solution of Stage 1, $\mathbf{r}_G(\tau_i)$. Because the first maneuver location is not controllable, it is omitted from these constraints. Note that if $\tau_k < t_f$, $\mathbf{x}_G(\tau_k)$ (the state immediately after at the k^{th} and final burn) is related to the goal final condition $\mathbf{x}(t_f)$ simply by the natural dynamics mapping $\mathbf{x}(\tau_k) = \psi^{-1}(\mathbf{x}(t_f), t_f, \tau_k)$. The second set of constraints, between dashed lines, enforce the kinematic constraint that changes in the monomial states at burn nodes (implicitly the result of impulsive maneuvers) should not instantaneously change the position. Note that the very first one is written differently to emphasize that $\mathbf{c}_j(\tau_0)$ is uncontrollable and thus does not appear in the free variables \mathbf{X} . Lastly, the final listed constraint in $\mathbf{F}(\mathbf{X})$ is enforcing that the final goal velocity, immediately after the k^{th} and final burn, is achieved.

The constraint Jacobian, $G(\mathbf{X}) = \frac{\partial}{\partial \mathbf{X}}(\mathbf{F}(\mathbf{X}))$, is computed analytically, and its derivation from Eq. (46) is straightforward:

$$G(\mathbf{X}) = \begin{bmatrix} 0_{\frac{N}{2} \times N} & \Psi_{r,j}(\tau_2)C_{j,2} & 0_{\frac{N}{2} \times N} & 0_{\frac{N}{2} \times N} & \dots & 0_{\frac{N}{2} \times N} & 0_{\frac{N}{2} \times N} \\ 0_{\frac{N}{2} \times N} & 0_{\frac{N}{2} \times N} & \Psi_{r,j}(\tau_3)C_{j,3} & 0_{\frac{N}{2} \times N} & \dots & 0_{\frac{N}{2} \times N} & 0_{\frac{N}{2} \times N} \\ & & \vdots & & & & \\ 0_{\frac{N}{2} \times N} & 0_{\frac{N}{2} \times N} & 0_{\frac{N}{2} \times N} & 0_{\frac{N}{2} \times N} & \dots & 0_{\frac{N}{2} \times N} & \Psi_{r,j}(\tau_k)C_{j,k} \\ \hline \Psi_{r,j}(\tau_1)C_{j,1} & 0_{\frac{N}{2} \times N} & 0_{\frac{N}{2} \times N} & 0_{\frac{N}{2} \times N} & \dots & 0_{\frac{N}{2} \times N} & 0_{\frac{N}{2} \times N} \\ -\Psi_{r,j}(\tau_2)C_{j,1} & \Psi_{r,j}(\tau_2)C_{j,2} & 0_{\frac{N}{2} \times N} & 0_{\frac{N}{2} \times N} & \dots & 0_{\frac{N}{2} \times N} & 0_{\frac{N}{2} \times N} \\ 0_{\frac{N}{2} \times N} & -\Psi_{r,j}(\tau_3)C_{j,2} & \Psi_{r,j}(\tau_3)C_{j,3} & 0_{\frac{N}{2} \times N} & \dots & 0_{\frac{N}{2} \times N} & 0_{\frac{N}{2} \times N} \\ & & \vdots & & & & \\ 0_{\frac{N}{2} \times N} & 0_{\frac{N}{2} \times N} & 0_{\frac{N}{2} \times N} & 0_{\frac{N}{2} \times N} & \dots & -\Psi_{r,j}(\tau_k)C_{j,k-1} & \Psi_{r,j}(\tau_k)C_{j,k} \\ 0_{\frac{N}{2} \times N} & 0_{\frac{N}{2} \times N} & 0_{\frac{N}{2} \times N} & 0_{\frac{N}{2} \times N} & \dots & 0_{\frac{N}{2} \times N} & \Psi_{v,j}(\tau_k)C_{j,k} \end{bmatrix} \quad (47)$$

where $C_{j,i} = \left. \frac{\partial c_j}{\partial c_1} \right|_{c_1(\tau_i)}$ which can be computed analytically by exploiting the known monomial structure of the c_j . This $kN \times kN$ matrix is full rank for our problem of interest. Thus the Newton step can be assessed as below:

$$\delta \mathbf{X} = -\gamma G^{-1} \mathbf{F}(\mathbf{X}), \quad 0 < \gamma \leq 1 \quad (48)$$

The proper γ can, if needed, be chosen by evaluating the error norm of $\mathbf{F}(\mathbf{X} + \delta \mathbf{X})$ for a pre-determined sequence of γ , i.e. in a line-search, because of the extremely low overhead in computing $\mathbf{F}(\mathbf{X})$. For our examples, the simple choice $\gamma = 1$ was always sufficient. This linear problem is initialized by constructing $\mathbf{X}^{(0)}$ (i.e. the 0th iteration) directly from the $c_1(\tau_i)$ outputs from Stage 1 of guidance. Because there is no need for any complicated numerics in the analytic computations of Eqs. (47) and (48), Stage 2 is extremely rapid. In our experience, the total time taken by all needed successive corrections of Stage 2 are much faster than the small SOCP solved by stage 1.

We now apply the aforementioned procedure to an example short-range low-Earth orbit (LEO) rendezvous and proximity operations scenario. For this example, a linearized rendezvous trajectory is generated which requires correction for the nonlinear dynamics of relative motion in low-Earth orbit. The problem details are provided in Table 1. Also included in that table are the runtime details for generation of the nonlinear fundamental solutions in Ψ_j via a differential algebra scheme. These are computed once, and reused for the first two examples in this paper. Note that instead using numerically propagated STTs, the compute times for each order were much slower, ~ 129 s (3), 6.69s (2), and 0.747s (1). Also, for this particular problem there exist analytic nonlinear expansions in literature. In particular, exact nonlinear expansions suitable for computing $\Psi_j(t)$ up to order $j = 3$ can be found (in normalized form) in Butcher et al. (2016). See also Butcher et al. (2017) and Willis et al. (2019b) and also references therein. Such analytic solutions unburden onboard algorithms from any onboard numerical integration to render the nonlinear fundamental solutions. More details can be found in Appendix A.

Table 1: Parameters for Rendezvous Example 1

Parameter	Values
Target spacecraft	LEO orbit, $a = 6378$ km, $e = 0$, $T \approx 1.4$ hrs
Control interval	$t_0 = 0.1T$, $t_f = 2.3T$, discretized into 220 times
Relative state, $t = 0$	$\mathbf{x}(0) = [-1266.6, -12000, 1000, 0, 2.9748, 0]$ (units: m, m/s)
Relative state, t_f	$\mathbf{x}(t_f) = [-589.6, 383.2, -1825.9, 2.3747, 1.4617, -1.3499]$
STT info	Duration: $2.3T$. Discretization: 230 times. Size: 474 kb Compute time (order): 0.795s (3), 0.349s (2), 0.175s (1)
Linear guidance	Burn indices: [0, 93, 142, 201, 219]. Delta-V: 2.336 m/s. Runtime: 0.108s
Stage 2 guidance	Delta-V: 2.353 m/s. Runtime: 0.0119s

Figure 6 gives the nominal guidance solution produced by Stage 1, propagated with the linearized dynamics assumed therein (in this case, the CW dynamics). This is generated on a 2023 MacBook Pro (M2 chip) in Python 3, using CVXPY (Diamond and Boyd, 2016; Agrawal et al., 2018) with ECOS (Domahidi et al., 2013) to solve the SOCP in ~ 0.1 s. After a sequence of 5 burns, the goal state is achieved: entry onto a tilted target-centered relative orbit. This linearized guidance solution requires a maneuver sequence with a total delta-V of 2.336 m/s. In subsequent figures the nominal linear guidance solution appears as a gray curve.

To produce Figure 7, the original Stage 1 guidance solution (nominal delta-Vs applied at pre-planned times) is followed in an open-loop fashion subject to the nonlinear dynamics – in other words, the initial condition is integrated and the nominal impulsive guidance strategy is followed at the pre-computed maneuver times by stopping integration, adding the impulse, and resuming integration to the next impulse. This yields the orange curve. With no allowance for corrective maneuvers, the goal state is clearly not achieved. This illustrates a well-known limitation of using linearized dynamics for rendezvous guidance: the nominal trajectories predicted by linearization will have to be corrected for accuracy in a high-fidelity model. There are various means of doing this, such as refinement via successive convexification, post-processing with sequential Lambert targeting (restricted to two-body problems), or correction via multiple-shooting schemes. These come at some non-trivial computational cost that must be paid each time a new trajectory is devised.

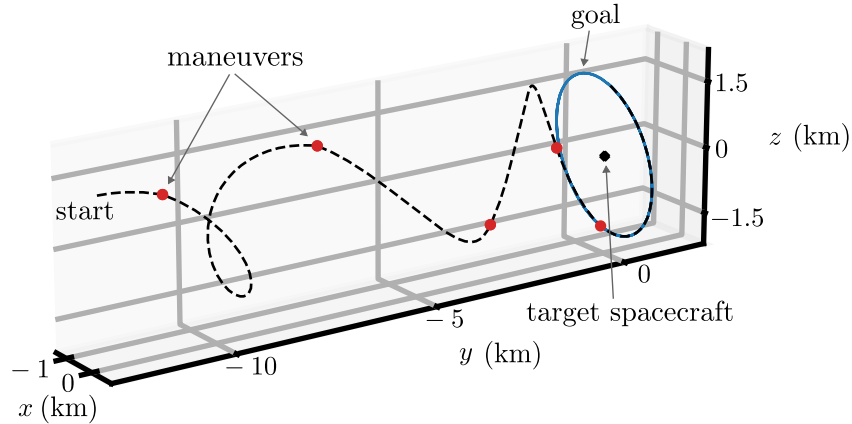


Figure 6: Nominal linear guidance trajectory, linearized dynamics (rendezvous ex. 1)

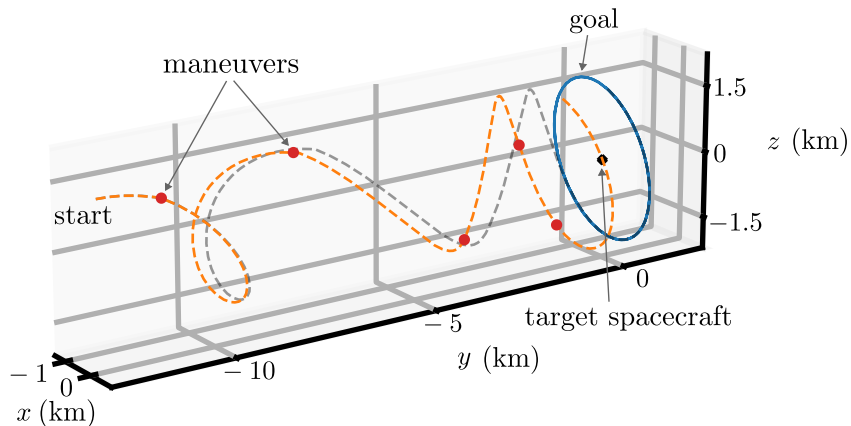


Figure 7: Executed open-loop linear guidance, nonlinear dynamics (rendezvous ex. 1)

In Figure 8, we show the results of Stage 2. This correction is achieved in ~ 0.01 s with 2 iterations of the Newton solver scheme (~ 0.005 s per iteration) – making use of analytic monomial expressions and the pre-saved $\Psi_j(t)$ evaluated at the critical times. The resulting nominal trajectory is again simulated in open-loop with the nonlinear dynamics, but now satisfies the final conditions to a high degree of accuracy (0.37% error in final along-track position, $< 0.1\%$ error in all other states). In our tests, we find that this two-stage guidance scheme is quite stable, even when the linearized initial guess (Stage 1) is highly erroneous.

4.2 Nonlinear spacecraft rendezvous in LEO – Successive convexification-based optimal guidance

Now we provide a simple demonstration of the successive convexification scheme introduced in Section 3.2. For this example we consider a new LEO rendezvous case whose details are provided in Table 2. This example combines medium range along-track separation with some out-of-plane motion which must be regulated to achieve a final stationary along-track state with 1.5 km offset from the target spacecraft. As before, we first compute a linearized guidance solution (Stage 1) and then a nonlinear guidance solution (now via the SCP scheme). The linearized guidance solution, and its failed open-loop execution, are depicted in Figure 9. This solution is computed in ~ 0.05 s.

Figure 10 gives the nonlinear guidance solution obtained via the SCP framework, minimizing sum of delta-V norm squared, thus $\mathcal{P} = 2$, where the burn nodes and delta-V vectors are allowed to change via implementation of the scheme discussed in Section 3.2. To facilitate the most rapid solution we inherit

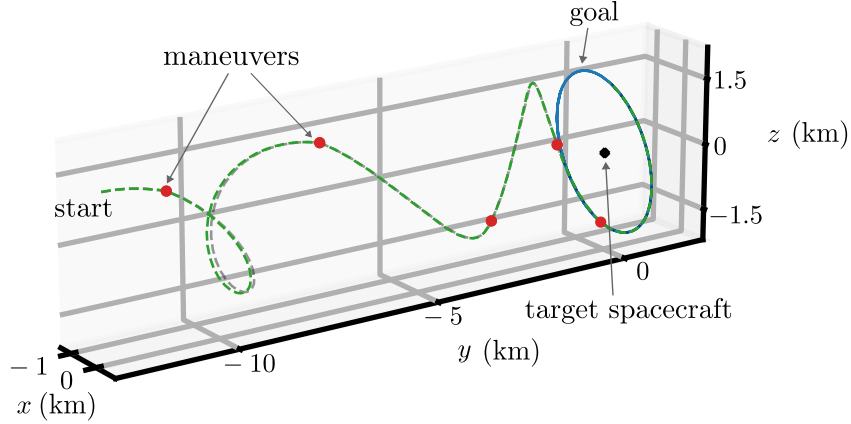


Figure 8: Executed open-loop nonlinear guidance, nonlinear dynamics (rendezvous ex. 1)

Table 2: Parameters for Rendezvous Example 2a (Min. sum of delta-V squared, $\mathcal{P} = 2$)

Parameter	Values
Target spacecraft	LEO orbit, $a = 6378$ km, $e = 0$, $T \approx 1.4$ hrs
Control interval	$t_0 = 0.1T$, $t_f = 1.1T$, discretized into 4 points (burn times fixed)
Relative state, $t = 0$	$\mathbf{x}(0) = [-3666.7, -62000, -4000, -1.239, 7.437, 2.479]$ (units: m, m/s)
Relative state, t_f	$\mathbf{x}(t_f) = [0, 1500, 0, 0, 0, 0]$
STT info	Reused from Example 1
Linear guidance	Burn indices: $[0, 12, 64, 99]$. Δv : 10.04 m/s. Runtime: 0.052s Open-loop error: >10 km range, trajectory failed
SCP guidance	Δv : 10.82 m/s. Runtime: 0.1s. Open-loop t_f error: 0.0529 km, 6.0 cm/s
SCP parameters	Fixed trust region, $d = 3$. Slack penalty weight $w = 20$. Method: ECOS Convergence condition: $\ \tilde{\mathbf{X}}\ < 10^{-4}$, No. iterations needed: 5

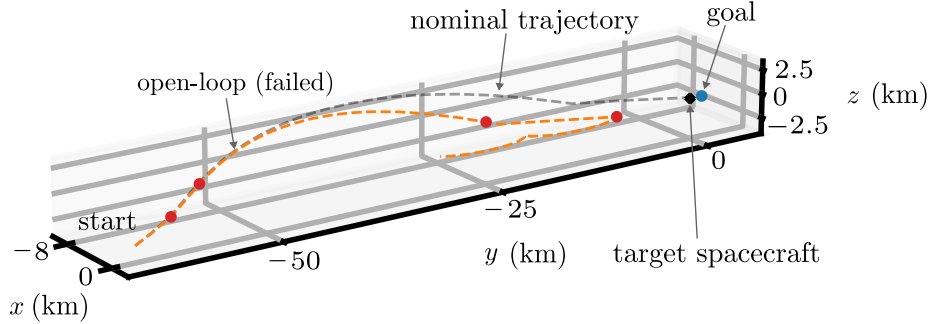


Figure 9: Executed open-loop linear guidance, nonlinear dynamics (rendezvous ex. 2a)

the optimal burn times of the linearized guidance solution, which minimizes the dimensionality of decision variables (although the SCP framework allows for the times to be optimized as well). The SCP solution, which is generated using the linearized guidance solution as an initial guess, converges in 5 iterations in a total runtime of ~ 0.1 s, with a runtime per iteration of ~ 0.02 s. The total solve time (linear SOCP + nonlinear SCP) to generate this nonlinear guidance solution was thus ~ 0.15 s. The resulting guidance solution requires 10.82 m/s of total delta-V, compared to the linearized prediction of 10 m/s, and a two-stage guidance requirement of 11.2 m/s. In open-loop execution with the nonlinear dynamics, the guidance solution results in very modest final state error (as shown in Table 2), reflecting the limits of accuracy of the map Ψ_j for order $j = 3$ with the monomials defined in the Cartesian coordinates. For completeness, Figures 11

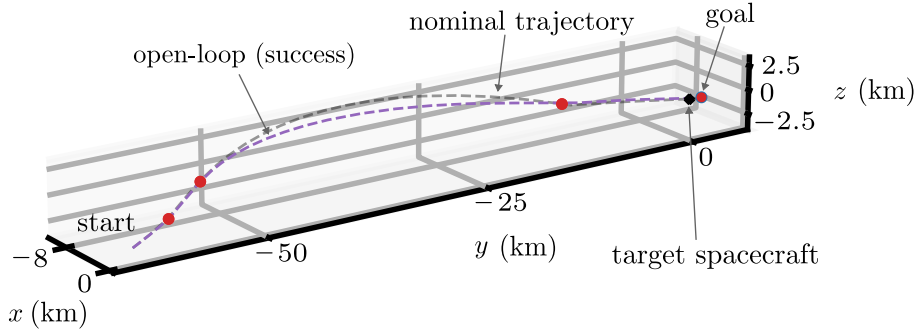


Figure 10: Executed open-loop SCP-based guidance, nonlinear dynamics (rendezvous ex. 2a)

and 12 give the norm of the (non-slack) free variables, $\|\tilde{\mathbf{X}}\|$, and the total cost J vs. iteration number. The steady drop in the norm of the free variables per iteration, as well as decreasing cost, correspond with our expectations of nominal behavior of the SCP scheme converging to a feasible minimum. For this problem, the norm of the vector of slack variables, $\|\mathbf{S}\|$, never exceeded 10^{-6} .

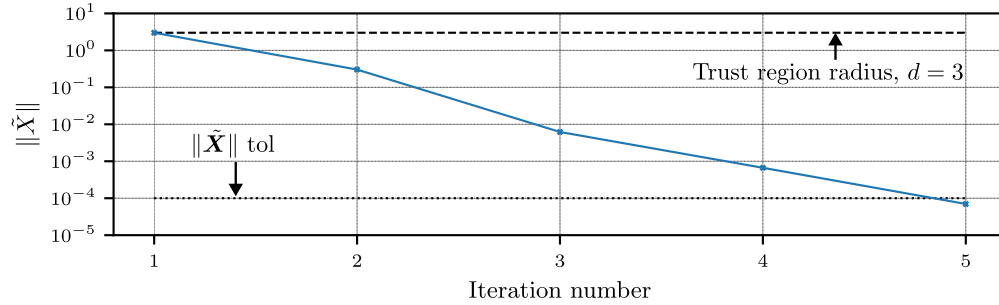


Figure 11: SCP norm of non-slack free vars. vs. iter no. (rendezvous ex. 2a)

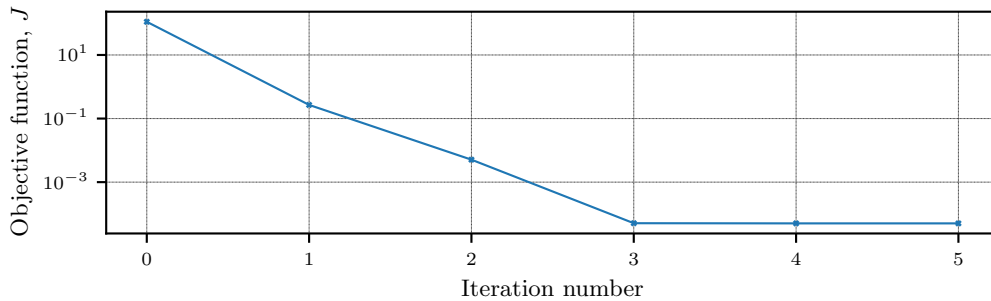


Figure 12: SCP total cost vs. iter no. (rendezvous ex. 2a)

For this same problem, we also compute via SCP the $\mathcal{P} = 1$ delta-V minimizing solution, and in addition we allow for the burn times to be selected from 100 candidate discretization points. The details for the new solver scheme are given in Table 3. The final SCP solution still has only 4 maneuvers, but the timing of the inner two is shifted slightly. The other discretization times are automatically identified (as a by-product of the geometrically optimal path on $\mathcal{C}^{(N)}$) to be sub-optimal burn times, so the optimal result gives only 4 non-null jumps in the $\mathbf{c}_j(t_i)$ across the 100 discretizations of the path. Note the increase in runtime to 2.5s as a result of the twenty-five fold expansion of the dimensionality of free variables for this example. The nominal delta-V is also slightly reduced. Figure 13 gives the new guidance solution, with the SCP solution

in purple, the discretization of the problem shown by the gray dots (showing only 50 of the 100 points for clarity), and the selected burn nodes shown as red dots.

Table 3: Parameters for Rendezvous Example 2b (Min. sum of delta-V, $\mathcal{P} = 1$)

Parameter	Values
Target spacecraft	LEO orbit, $a = 6378$ km, $e = 0$, $T \approx 1.4$ hrs
Control interval	$t_0 = 0.1T$, $t_f = 1.1T$, discretized into 100 points (burn times free)
Linear vs. SCP	Burn indices: Linear, [0, 12, 64, 99]. SCP solution, [0, 13, 65, 99]
SCP guidance	Δv : 10.73 m/s. Runtime: 2.5s. Open-loop t_f error: 0.108 km, 14.6 cm/s
SCP parameters	Fixed trust region, $d = 10$. Slack penalty weight $w = 5$. Method: ECOS Convergence condition: $\ \tilde{\mathbf{X}}\ < 10^{-4}$, No. iterations needed: 6

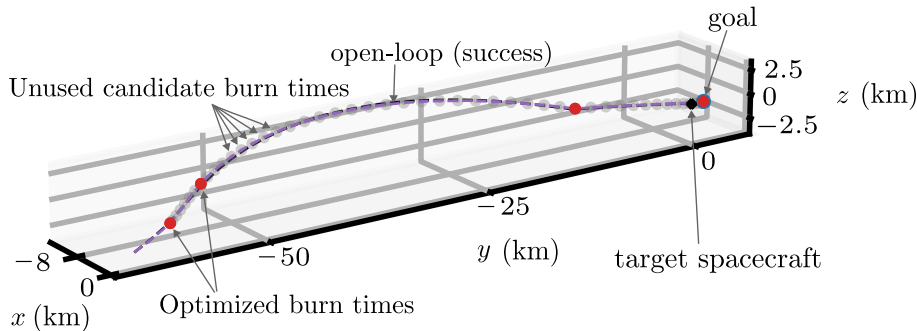


Figure 13: Executed open-loop SCP-based guidance, nonlinear dynamics (rendezvous ex. 2b)

All guidance examples shown so far were generated using the same pre-computed third order nonlinear expansion, and represent a small sample of the trade space that can be explored leveraging that same data. The two-stage nonlinear guidance and SCP-based nonlinear guidance implementations all perform without the need for any real-time numerical integration, and their robustness to starting with a poor linearization-based initial guess is encouraging and interesting. Both offer nonlinear correction in a comparable amount of time that was required to generate the linearized initial guess, but of course the SCP-based implementation comes with the added delta-V minimizing benefit. Note that our implementation in Python is not optimized for speed but for proof of concept, and a CVXPYgen implementation of the SCP could potentially improve performance by removing significant overhead from successive CVXPY calls (Schaller et al., 2022).

4.3 Long range rendezvous guidance via spherical coordinate monomials

In solving the trajectory optimization problem, any desired working coordinates can be used in the construction of the \mathbf{c}_j and the computation of their associated fundamental solution matrix Ψ_j . For orbital mechanics problems, it is well-known that curvilinear/spherical coordinates yield a lower level of dynamical nonlinearity than the Cartesian coordinates (Willis et al., 2019b; Junkins, 1997). In other words, for a given order j , the Ψ_j computed in spherical coordinates will have a greater physical region of validity than its counterpart in Cartesian coordinates. In this section we modify the previous guidance implementation, instead now making use of a spherical coordinate overparameterized monomial representation. The result is a solver with a much greater region of validity ($\mathcal{O}(1000)$ km in LEO for order $j = 3$, as opposed to $\mathcal{O}(100)$ km for the third-order Cartesian representation).

The relative position can be developed in relative spherical coordinates $\delta r, \delta \theta, \delta \phi$, which relate to the Cartesian relative position coordinates as:

$$\begin{aligned}
 x &= (r + \delta r) \cos \delta \theta \cos \delta \psi - r \\
 y &= (r + \delta r) \sin \delta \theta \cos \delta \phi \\
 z &= (r + \delta r) \sin \delta \phi
 \end{aligned} \tag{49}$$

where r is the instantaneous target orbit radius, $r_c = r + \delta r$ is the instantaneous chaser orbit radius, $\delta\theta$ is an Earth-centered angular offset measured in the plane of the target orbit, and $\delta\phi$ is the out of plane angular offset. The derivatives of these quantities, $\delta\dot{r}$, $\delta\dot{\theta}$, $\delta\dot{\phi}$, constitute the remainder of the state description, and the Cartesian velocities relate to the spherical relative states as below:

$$\begin{aligned}\dot{x} &= (\dot{r} + \delta\dot{r}) \cos \delta\phi \cos \delta\theta - (r + \delta r)(\delta\dot{\phi} \sin \delta\phi \cos \delta\theta + \delta\dot{\theta} \cos \delta\phi \sin \delta\theta) - \dot{r} \\ \dot{y} &= (\dot{r} + \delta\dot{r}) \cos \delta\phi \sin \delta\theta - (r + \delta r)(\delta\dot{\phi} \sin \delta\phi \sin \delta\theta - \delta\dot{\theta} \cos \delta\phi \cos \delta\theta) \\ \dot{z} &= (\dot{r} + \delta\dot{r}) \sin \delta\phi + (r + \delta r)\delta\dot{\phi} \cos \delta\phi\end{aligned}\quad (50)$$

Using the notation of Section 2.5.2, these define new working coordinates, $\boldsymbol{\eta} = (\delta r, \delta\theta, \delta\phi, \delta\dot{r}, \delta\dot{\theta}, \delta\dot{\phi})^\top$. See e.g. Willis et al. (2019a) for the full inverse mapping between Cartesian and spherical coordinates. For convenience we use the normalized spherical relative coordinates $\bar{\boldsymbol{\eta}} = (\delta\rho, \delta\theta, \delta\phi, \delta\rho', \delta\theta', \delta\phi')^\top$. The radial coordinates are normalized by $\delta\rho = \delta r/a$, and we normalize time as $\tau = nt$, thus $(\cdot)' = \frac{d}{d\tau}(\cdot) = \frac{1}{n} \frac{d}{dt}(\cdot)$.

We develop code to compute new maps $\Psi_j(t)$ that contain the nonlinear fundamental solutions for the following 3D (6 state) normalized target-centered spherical coordinate nonlinear dynamics of Keplerian relative motion:

$$\delta\rho'' = \frac{1}{\rho^2} - \frac{1}{(\rho + \delta\rho)^2} - \rho\theta'^2 + (\rho + \delta\rho)(\delta\phi'^2 + (\theta' + \delta\theta')^2 \cos^2 \delta\phi) \quad (51a)$$

$$\delta\theta'' = 2\frac{\rho'\theta'}{\rho} - 2\frac{\rho' + \delta\rho'}{\rho + \delta\rho}(\theta' + \delta\theta') + 2(\theta' + \delta\theta')\delta\phi' \tan \delta\phi \quad (51b)$$

$$\delta\phi'' = -2\frac{\rho' + \delta\rho'}{\rho + \delta\rho}\delta\phi' - (\theta' + \delta\theta')^2 \cos \delta\phi \sin \delta\phi \quad (51c)$$

These are integrated in parallel with the normalized 2D (4 state) equations of the target orbit:

$$\rho'' = -\frac{1}{\rho^2} + \rho\theta'^2 \quad (52a)$$

$$\theta'' = -2\frac{\rho'\theta'}{\rho} \quad (52b)$$

where ρ is the target orbital radius and θ its argument of latitude. This normalization scheme allows the same Ψ_j to be reused for rendezvous guidance for all target orbits of a given eccentricity, regardless of the target semimajor axis. This enables all circular Keplerian rendezvous guidance problems of a given maximum normalized duration, discretization, and scale to be handled using the same pre-computed information. Using Eq. (50) and the normalization definition, and denoting the transformation from normalized spherical states to dimensional Cartesian velocity as $\boldsymbol{v} = \boldsymbol{g}_v(\bar{\boldsymbol{\eta}})$, the delta-V resulting from a given impulsive change in the normalized spherical coordinates can be defined:

$$\Delta\boldsymbol{v}(t_i) = \boldsymbol{g}_v(\bar{\boldsymbol{\eta}}(t_i^+)) - \boldsymbol{g}_v(\bar{\boldsymbol{\eta}}(t_i^-)) \quad (53)$$

with t_i^- and t_i^+ denoting the state just before and after the maneuver. This is a complex *nonlinear* function of the normalized spherical coordinates, but it admits (approximately) the following linear relationship to the overparameterized spherical monomial states, computed using differential algebra:

$$\Delta\boldsymbol{v}(t_i) = \Gamma_{v,j}(t_i) \left(\boldsymbol{c}_j^{(\bar{\boldsymbol{\eta}})}(t_i) - \boldsymbol{c}_j^{(\bar{\boldsymbol{\eta}})}(t_{i-1}) \right) \quad (54)$$

This transformation renders delta-V norm and norm-squared cost functions convex in $\boldsymbol{c}_j^{(\bar{\boldsymbol{\eta}})}$. As for problem constraints, we require that impulsive maneuvers change only the velocity components $\delta\rho'$, $\delta\theta'$, $\delta\phi'$ without affecting the position components $\delta\rho$, $\delta\theta$, $\delta\phi$. As a result, the kinematic constraints are otherwise still handled by the Ψ_j (but now developed for the spherical monomials), and a spherical coordinate equivalent of the SCP scheme defined in Eq. (30) modifies only the cost terms, with a substitution of $\Gamma_{v,j}(t_i)$ for the $\Psi_{v,j}(t_i)$.

Table 4 gives some info about the maps Ψ_j computed for the spherical monomials using differential algebra methods. We compute up to order $j = 4$, and note at order $j = 2$ that we recover numerically the analytic

finding of Willis et al. (2019a) that of 21 possible second-order fundamental solutions (reflecting the 21 different quadratic monomials), only 15 are nonzero. This is opposed to the Cartesian coordinate solution, for which 19 are nonzero. Thus the spherical coordinate parameterization is more compact. This property extends to order $j = 4$, at which point of the 209 possible fundamental solutions, corresponding with all unique monomials from orders 1 to 4, 83 are zero. We also determine that the computation speed of the map is not greatly affected by eccentricity, but more eccentric cases require a finer discretization in the integration of Eqs. (51) and Eq. (52) to keep the same level of accuracy. Due to the normalization, a computed map of given eccentricity applies for any target semimajor axis and orbit period, about any planet. Equivalent maps could be constructed for different eccentricities, or for altogether different dynamical regimes, but we continue with the classic circular orbit case $e = 0$ studied most frequently in the spacecraft rendezvous community. We write a new SCP solver using the normalized spherical coordinates as our working coordinates for the monomial basis. The normalization also standardizes the choice of (normalized) trust region d vs. order j , so that spacecraft rendezvous expertise is no longer required in choosing this value.

Table 4: Developing the Fundamental Solution Matrix for Various Cases

Parameter	Values
Discretization info	$\Delta\tau = 4\pi$ (2 target orbits), discretized into 400 points
Circular orbit ($e = 0$)	Compute time (order j): 3.2s (4), 1.4s (3), 0.6s (2), 0.1s (1) Data size: 2.96 MB, number of empty columns of Ψ_j for $j = 4$: 83
Eccentric orbit ($e = 0.2$)	Compute time (order j): 3.2s (4), 1.4s (3), 0.6s (2), 0.3s (1) Data size: 3.04 MB, number of empty columns of Ψ_j for $j = 4$: 83

Consider the long-range case described in Table 5. The chaser spacecraft is initialized in an orbit of a similar period but phased over 2000 km behind the target spacecraft, with some additional out-of-plane motion that must be regulated. The control problem is to reduce the inter-spacecraft separation to a purely along-track separation of 10 km, whereupon terminal rendezvous procedures can later be initiated. Of the 400 saved times for the map Ψ_j , this data is down-sampled by a factor of three to define a control problem with a reasonable number of candidate burn times. To cover the large distance in just under 2.5 hours, the optimal solution will use much more delta-V than the earlier examples. We provide two solutions. The first solution, depicted in Figure 14, uses the two-stage guidance scheme to produce a dynamically feasible initial guess of the optimal transfer, which is then corrected using the SCP scheme. The linearly predicted optimal burn times are inherited, but the location and delta-V vector of these burn nodes is adjusted via the SCP. For the second solution, given by Figure 15, the two-stage guidance solution is corrected with the burn times left free, and the SCP scheme changes the timing of the burns slightly (each <5 discretized times away from all nominal burns). The result is a slightly different shape to the trajectory: observe the “kink” during which the relative motion trajectory greatly slows down, as evidenced by the clustering of discretization points which are chosen uniformly in time for this example.

Table 5: Simulation Parameters for Rendezvous Example 3 (Min. sum of delta-V, $\mathcal{P} = 1$)

Parameter	Values
Target spacecraft	LEO orbit, $a = 6378$ km, $e = 0$, $T \approx 1.4$ hrs
Control interval	$t_0 = 0.05T$, $t_f = 1.80T$, discretized into 118 points
Relative state, $t = 0$	$\mathbf{x}(0) = [-320.4, -2000, 70, 0, -5n, 10n]$ (units: km, km/s), $n = 2\pi/T$
Relative state, t_f	$\mathbf{x}(t_f) = [0, -10, 0, 0, 0, 0]$

Table 6 gives the guidance solution info, as well as runtime and open-loop execution error for the $j = 4$ solutions. In comparison to these results, note that $j = 3$ produced a highly similar guidance solution, but also resulted in final state targeting range error of ~ 1 km. While this is an error on the scale of $\sim 0.05\%$ in terms of the initial range, it is a $\sim 10\%$ error in the much smaller goal range, necessitating the extra order to bring this error below 1%. The $j = 4$ solution required only $\sim 47\%$ more compute time than $j = 3$. Note in both SCP solutions, the nonlinear optimal solution removes the need for the linearly predicted optimal burn

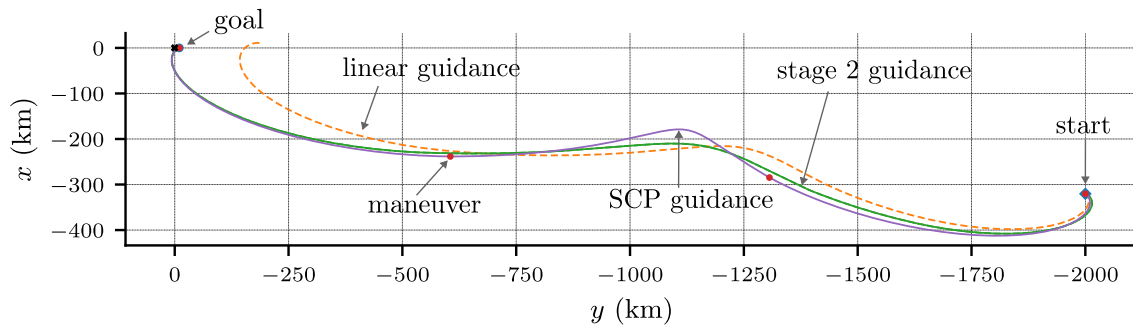


Figure 14: Executed open-loop guidance, SCP with inherited burn times (rendezvous ex. 3a)

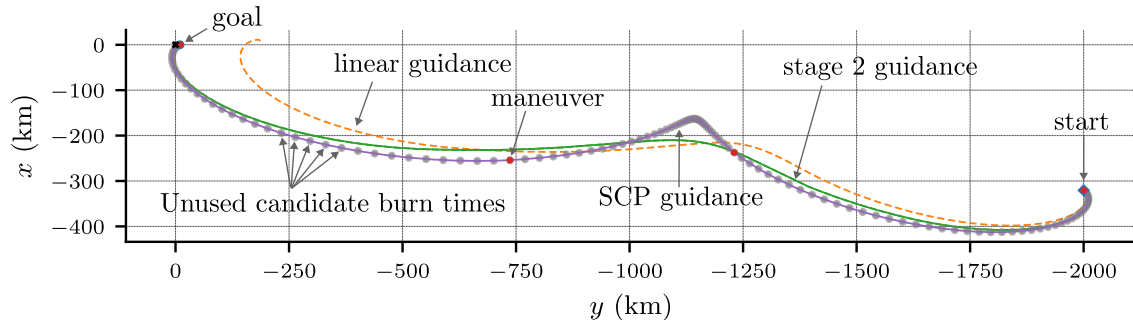


Figure 15: Executed open-loop guidance, SCP with free burn times (rendezvous ex. 3b)

Table 6: Guidance Results for Rendezvous Example 3

Parameter	Values
Two-stage guidance	Burn indices: [0, 30, 40, 83, 116]. Δv : 243.00 m/s. Total runtime: 0.128s Open-loop error (pos/vel norm): 0.645 km, 0.356 m/s; No. iterations needed: 3 (which took 0.054s)
SCP parameters	Fixed trust region, $d = 0.1$. Slack penalty weight $w = 10^3$. Method: ECOS Convergence condition: $\ \tilde{\mathbf{X}}\ < 10^{-7}$ (note: problem normalized)
SCP (fixed burn times)	Burn indices: [0, 40, 83, 116]. Δv : 226.31 m/s. Runtime: 0.296s Open-loop end error (pos/vel norm), $j = 4$: 0.038 km, 0.193 m/s; No. iterations needed: 6
SCP (free burn times)	Burn indices: [0, 44, 81, 117]. Δv : 222.22 m/s. Runtime: 3.89s Open-loop end error (pos/vel norm), $j = 4$: 0.0857 km, 0.332 m/s; No. iterations needed: 10

at index 30 entirely. However the two-stage guidance already provides a decent solution, with SCP results only reducing total delta-V on the order of 10%. In comparing the SCP solution which inherits the linearly optimal burn times to the solution with burn times free, note that the burn times are shifted slightly, the delta-V is decreased by another $\sim 2\%$, but the runtime is over 10 times longer due to a similar expansion in the number of decision variables. Overall, this demonstration illustrates a few concepts: 1) the importance of choice of working coordinates for the monomials and the superiority of spherical coordinates over Cartesian, 2) the usefulness of problem normalization, and 3) the increase in runtime with order j , which is much less than the growth of the dimensionality of the monomials, K_j .

4.4 Nonlinear state constraints

Finally, we apply a simple set of constraints to modify the prior example and show the property of embedding nonlinear constraints. We consider a series of constraints on the inter-spacecraft range as follows:

$$\varrho_{\min} = \begin{cases} 1915 \text{ km} & t \leq 0.4T \\ 1405 \text{ km} & 0.4T < t \leq 0.75T \\ 318 \text{ km} & 0.75T < t \leq 1.4T \\ 64 \text{ km} & 1.4T < t \leq 1.6T \\ 7.5 \text{ km} & t > 1.6T \end{cases} \quad (55)$$

These timed constraints emulate a simple active safety requirement, wherein the chaser spacecraft should not approach the target in a manner more aggressive than the specified approach stages. The inter-spacecraft range ϱ is related to the instantaneous spherical relative position coordinates $\delta r, \delta\theta, \delta\phi$ and the target orbital radius r by the following nonlinear expression:

$$\begin{aligned} \varrho &= \sqrt{\delta r^2 + 2r\delta r + 2r^2 - 2r(r + \delta r) \cos \delta\phi \cos \delta\theta} \\ &= a\sqrt{\delta\rho^2 + 2\rho\delta\rho + 2\rho^2 - 2\rho(\rho + \delta\rho) \cos \delta\phi \cos \delta\theta} \end{aligned} \quad (56)$$

Equivalently we can define the constraint $\varrho^2(t) \geq \varrho_{\min}^2(t)$ to avoid the needless square root for an always-positive function. Furthermore we can normalize the constraint as $\bar{\varrho}^2(t) \geq \bar{\varrho}_{\min}^2(t)$, with $\varrho = a\bar{\varrho}$. This constraint is nonlinear in the spherical relative coordinates, but via differential algebra we can impose this nonlinear constraint function as a linear constraint function on the $\mathbf{c}_j^{(\bar{\eta})}(t_i) \forall t_i$:

$$h(\bar{\boldsymbol{\eta}}(t_i)) = \bar{\varrho}^2(t_i) \quad (57a)$$

$$h(\bar{\boldsymbol{\eta}}(t_i)) \geq \bar{\varrho}_{\min}^2(t_i) \quad (57b)$$

$$h(\bar{\boldsymbol{\eta}}(t_i), t_k) = \boldsymbol{\gamma}_{h,j}^\top(t_k) \mathbf{c}_j^{(\bar{\eta})}(t_i) \quad (57c)$$

$$\boldsymbol{\gamma}_{h,j}^\top(t_k) \mathbf{c}_j^{(\bar{\eta})}(t_i) \geq \bar{\varrho}_{\min}^2(t_i) \quad (57d)$$

where $\boldsymbol{\gamma}_{h,j}(t_k)$ is computed from the normalized version of Eq. (56) using differential algebra, similarly to Ψ_j and $\Gamma_{v,j}$. This function provides the mapping from the monomial expansion $\mathbf{E}_j(\bar{\boldsymbol{\eta}}(0))$ to range at time t_k via the j^{th} -order truncation of the flow of the natural dynamics. Thus it is also possible via this formulation to enforce passive safety constraints, wherein states at time t_i are constrained based on their free-drift implications at times $t_k \geq t_i$, although this was not explored, and we enforce only instantaneous range at all trajectory nodes i.e. $t_k = t_i$.

Similarly to the kinematic constraints, Eq. (57) is linear in the $\mathbf{c}_j^{(\bar{\eta})}$, thus the same successive convexification procedure extends naturally to accommodate this extra constraint, given below as an addendum to Eq. (30):

$$\boldsymbol{\gamma}_{h,j}^\top(t_i) \left(\mathbf{c}_j^{(\bar{\eta})'}(t_i) + \frac{\partial \mathbf{c}_j^{(\bar{\eta})}}{\partial \mathbf{c}_1^{(\bar{\eta})}} \Big|_i \delta \mathbf{c}_1^{(\bar{\eta})}(t_i) \right) + s_{\text{ineq},i} \geq \bar{\varrho}_{\min}^2(t_i), \quad i = 1:K \quad (58)$$

where the prime notation is reused to denote the result of a prior iteration, and this constraint results in the introduction of an extra K slack variables, expanding the dimensionality of the free variable vector \mathbf{X} in the convex solver. These extra slack variables must also be penalized, necessitating the addition of the following cost term:

$$\delta J_{\text{ineq}} = \mathbf{s}_{\text{ineq}}^\top P_{w,\text{ineq}} \mathbf{s}_{\text{ineq}} \quad (59)$$

where \mathbf{s}_{ineq} is a vector of just the scalar inequality slack variables $s_{\text{ineq},i}$, and $P_{w,\text{ineq}}$ is a diagonal positive-definite matrix whose diagonal elements can be chosen so that all slack variables are given equal treatment.

Applying the modified SCP scheme with path constraints as specified in Eq. (55), the inter-spacecraft range is given in Figure 16. This figure depicts the time-dependent range constraints, showing the unconstrained result equivalent to Example 3(b), and the new result which satisfies the range constraints. We note the

interesting addition of multiple burns at the end of the trajectory to avoid violation of the final range constraint of $\varrho_{\min} = 7.5$ km, which was previously violated. The satisfactory constrained trajectory is obtained with a total delta-V of 239.66 m/s, a 7.8% increase on the unconstrained case. The new scheme converges in 9 iterations with a solve time of 5.86s, achieving final position and velocity error norms of 0.092 km and 0.155 m/s, of similar targeting performance to the prior unconstrained $j = 4$ results. Note that additional modifications could be made to the solver to avoid returning sequences of small maneuvers – this is a consequence of our problem formulation and our simple delta-V minimizing cost function. The adjacent burns can usually be combined for fairly small delta-V penalty. Overall this example illustrates the inclusion of nonlinear state constraints into our new methodology, and we reserve more refined solver development to future work.

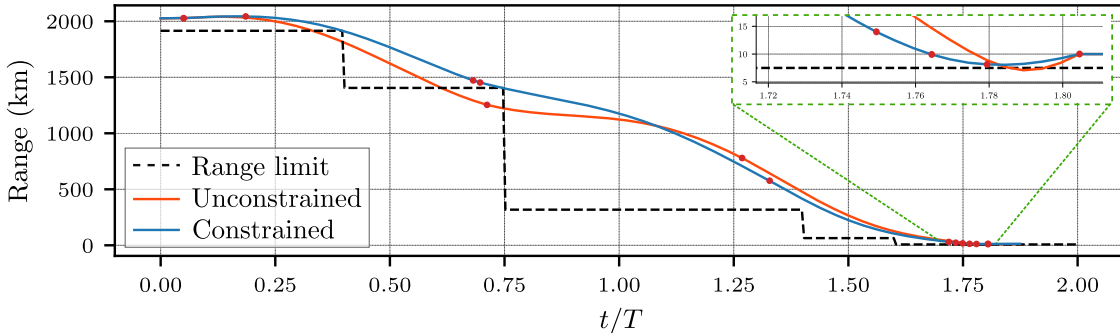


Figure 16: Inter-spacecraft range, unconstrained and constrained (rendezvous ex. 3c)

5 Conclusions

This paper introduces a method of rapid guidance for nonlinear systems leveraging overparameterized monomial coordinates and fundamental solution expansions. In essence, we trade nonlinearities and non-convexities of the original problem for a single non-convexity of our own design, posing the problem on the non-Euclidean surface $\mathcal{C}^{(N)}$ of known structure. By this methodology, trajectory optimization problems can be solved as path planning problems with very low real-time computational footprint. The solutions inherit the accuracy of the nonlinear fundamental solution expansions encoded by the special nonlinear fundamental solution matrix $\Psi_j(t)$. This is in contrast to collocation-based SCP schemes which have no guarantee of physical feasibility. We devise a simple two-stage (linear predict, nonlinear correct) approach and a simple successive convexification scheme to demonstrate the usefulness of the methodology. The spacecraft relative motion and rendezvous problem (and relatedly, orbit regulation) are particularly well-suited for this approach because the reference trajectory needed for the nonlinear solution expansions is clear: the target spacecraft orbit. We present several examples where our methodology is used to rapidly compute guidance solutions that are effective when propagated in a numerical model of nonlinear problem dynamics.

In general, like linear methods, this method is still only “locally” valid, though admitting a much larger domain of validity than linearization. For this reason, application to more general orbit transfer problems requires the computation of reasonable reference trajectories for the transfer, which are not always clear. It is also worth noting that, depending on order of nonlinearity j , the time to compute the fundamental solutions numerically can be non-negligible. We envision a GNC implementation where these solutions are computed hours, days, or more in advance of when needed in a mission. In the context of our chosen example problem of spacecraft rendezvous, incorporation of analytic or numerical fundamental solution expansions keeps the total computational footprint extremely low (solve times of $\mathcal{O}(1s)$ or shorter for our examples).

This is an early showcasing of a new methodology, where we only outline the fundamental ideas and provide simple examples. The opportunities for future work are significant. First, it is possible to extend this work to trajectory optimization problems with continuous thrust, the kinematic constraints of which were already

outlined. This will require a continuous interpolation of the discretized fundamental solution matrix $\Psi_j(t_i)$, which can be accomplished with splines, for example. Given an accurate continuous parameterization, we can also explore impulsive burn time flexibility in a continuous time context, as opposed to the discrete context in this work. This would be done by introducing the burn times as optimization variables, instead of relying on the convex solver to prevent sub-optimal transitions in the monomial states at all other discretization times. As such, the dimensionality of the problem could be greatly reduced, by a factor of 20 or so from the examples shown in this work. Additionally, incorporating more complex path constraints is straightforwardly inherited from more traditional implementations into our methodology because the relationship between the instantaneous state vector (or functions of the state vector) and its overparameterized monomial expression is linear.

There are some other future developments which require more theoretical work. For example, the error analysis outlined in this paper can and should be extended so that more formal guarantees on performance can be made. In this work, we merely provide early arguments towards that end, rooted in the fact that the feasible region for accurate use of our method is static. Relatedly, more advanced methods for sizing the trust region(s) should be explored, and indeed the trust region can be chosen to ensure the guidance solution remains in the domain of validity of its predictions. Extending this framework to accommodate stochasticity is also desirable for robust onboard applications. One possible path forward in this is provided by the fact the nonlinear fundamental solutions can also be expanded in terms of uncertain parameters. Because the non-convexities in this problem implementation are entirely due to the fact that the constraint surface $\mathcal{C}^{(N)}$ is non-Euclidean, and furthermore the constraint surface is analytically parameterized, it seems promising to leverage concepts from differential geometry to enhance the methodology. For example, local measures of curvature could directly inform the size of trust regions. Much more abstract are numerical techniques for optimization on manifolds themselves, exploiting the fact that the tangent space is locally homeomorphic to the manifold, wherein some familiar optimization concepts can perhaps be generalized. Indeed in our case, $\mathcal{C}^{(N)}$ is homeomorphic to \mathbb{R}^N within the entire domain of validity. The removal/reduction of our iterative solving procedure would greatly enhance the numerical performance of an already promising methodology.

Disclaimer

Funded by the European Union. Views and opinions expressed are however those of the authors only and do not necessarily reflect those of the European Union or the European Research Executive Agency. Neither the European Union nor the granting authority can be held responsible for them.

Acknowledgements

This work was performed as part of the MSCA project “Facilitating Autonomy in Astrodynamics for Spacecraft Technology”, Grant agreement ID: 101063274. We gratefully acknowledge technical and administrative support from the MSCA hosting organization: Department of Aerospace Science and Technology (DAER), Politecnico di Milano, Italy.

Code and Data Availability

Data and links to code to reproduce select examples from this paper will be made available via the open-access digital repository Zenodo at <https://zenodo.org/communities/faast-msca/about>.

References

- A. Agrawal, R. Verschueren, S. Diamond, and S. Boyd. A rewriting system for convex optimization problems. *Journal of Control and Decision*, 5(1):42–60, 2018. doi:10.1080/23307706.2017.1397554.

- A. W. Berning Jr., E. R. Burnett, and S. Bieniawski. Chance-constrained, drift-safe guidance for spacecraft rendezvous. In *AAS Rocky Mountain Guidance, Navigation, and Control Conference*. American Astronautical Society, 2023. doi:10.48550/arXiv.2401.11077.
- M. Berz. Chapter 2 - Differential Algebraic Techniques. In *Modern Map Methods in Particle Beam Physics*, volume 108 of *Advances in Imaging and Electron Physics*, pages 81–117. Academic Press, San Diego, CA, 1999. doi:10.1016/S1076-5670(08)70228-3.
- S. Boone and J. McMahan. Orbital Guidance Using Higher-Order State Transition Tensors. *Journal of Guidance, Control, and Dynamics*, 44(3):493–504, 2021. doi:10.2514/1.G005493.
- S. Boyd and L. Vandenberghe. *Convex Optimization*. Cambridge University Press, New York, 2004.
- E. R. Burnett and H. Schaub. Spacecraft relative motion dynamics and control using fundamental modal solution constants. *Journal of Guidance, Control, and Dynamics*, 45(10):1786–1799, 2022. doi:10.2514/1.G006603.
- E. R. Burnett, E. A. Butcher, A. J. Sinclair, and T. A. Lovell. Linearized Relative Orbital Motion Model About an Oblate Body Without Averaging. *Advances in the Astronautical Sciences*, 167(AAS 18-218): 691–710, 2018.
- E. A. Butcher, T. A. Lovell, and A. Harris. Third order cartesian relative motion perturbation solutions for slightly eccentric chief orbits. *Advances in the Astronautical Sciences*, 158(AAS 16-496):3435–3454, 2016. URL <https://www.scopus.com/inward/record.uri?eid=2-s2.0-85007356529&partnerID=40&md5=d2756042f95ce0dc7988721b36b77d3c>.
- E. A. Butcher, E. R. Burnett, and T. A. Lovell. Comparison of Relative Orbital Motion Perturbation Solutions in Cartesian and Spherical Coordinates. *Advances in the Astronautical Sciences*, (AAS 17-202), 2017.
- S. Casotto. The Equations of Relative Motion in the Orbital Reference Frame. *Celestial Mechanics and Dynamical Astronomy*, 124(3):215–234, 2016. doi:10.1007/s10569-015-9660-1.
- W. H. Clohessy and R. S. Wiltshire. Terminal Guidance System for Satellite Rendezvous. *Journal of the Aerospace Sciences*, 27(9):653–658, Sept. 1960. doi:10.2514/8.8704.
- G. Di Domenico, E. Andreis, A. C. Morelli, G. Merisio, V. Franzese, C. Giordano, A. Morselli, P. Panicucci, F. Ferrari, and F. Topputo. *The ERC-Funded EXTREMA Project: Achieving Self-Driving Interplanetary CubeSats*, pages 167–199. Springer International Publishing, Cham, 2023. ISBN 978-3-031-24812-2. doi:10.1007/978-3-031-24812-2.6.
- P. Di Lizia, R. Armellin, A. Morselli, and F. Bernelli-Zazzera. High order optimal feedback control of space trajectories with bounded control. *Acta Astronautica*, 94(1):383–394, 2014. doi:10.1016/j.actaastro.2013.02.011.
- S. Diamond and S. Boyd. CVXPY: A Python-embedded modeling language for convex optimization. *Journal of Machine Learning Research*, 17(83):1–5, 2016. doi:10.48550/arXiv.1603.00943.
- A. Domahidi, E. Chu, and S. Boyd. ECOS: An SOCP solver for embedded systems. In *2013 European Control Conference (ECC)*, pages 3071–3076. European Control Association, July 2013. doi:10.23919/ECC.2013.6669541.
- A. Giorgilli and M. Sansottera. Methods of algebraic manipulation in perturbation theory. *Workshop Series of the Asociacion Argentina de Astronomia*, 3:147–183, January 2011. doi:10.48550/arXiv.1303.7398.
- C. Greco, M. Di Carlo, M. Vasile, and R. Epenoy. Direct multiple shooting transcription with polynomial algebra for optimal control problems under uncertainty. *Acta Astronautica*, 170:224–234, 2020. doi:10.1016/j.actaastro.2019.12.010.
- T. Guffanti and S. D’Amico. Integration constants as state variables for optimal path planning. In *2018 European Control Conference (ECC)*, pages 1–6. European Control Association, June 2018. doi:10.23919/ECC.2018.8550448.

- E. J. Hinch. *Perturbation Methods*. Cambridge University Press, Cambridge, England, 1991. doi:10.1017/CBO9781139172189.
- C. Hofmann and F. Topputo. Rapid Low-Thrust Trajectory Optimization in Deep Space Based on Convex Programming. *Journal of Guidance, Control, and Dynamics*, 44(7):1379–1388, 2021. doi:10.2514/1.G005839.
- C. Hofmann, A. C. Morelli, and F. Topputo. On the Performance of Discretization and Trust-Region Methods for On-Board Convex Low-Thrust Trajectory Optimization. In *AIAA SCITECH 2022 Forum*, number 1892. AIAA, American Institute of Aeronautics and Astronautics, January 2022. doi:10.2514/6.2022-1892.
- C. Hofmann, A. C. Morelli, and F. Topputo. Performance assessment of convex low-thrust trajectory optimization methods. *Journal of Spacecraft and Rockets*, 60(1):299–314, 2023. doi:10.2514/1.A35461.
- D. Izzo, F. Biscani, C. Sánchez, J. Müller, and M. Heddes. `darioizzo/audi`: Update to the new `obake` API and `tbb` API (v1.9.2). Zenodo, June 2022.
- À. Jorba. A Methodology for the Numerical Computation of Normal Forms, Centre Manifolds and First Integrals of Hamiltonian Systems. *Experimental Mathematics*, 8(2):155–195, 1999. doi:10.1080/10586458.1999.10504397.
- J. L. Junkins. Adventures on the Interface of Dynamics and Control. *AIAA Journal of Guidance, Control, and Dynamics*, 20(6):1058–1071, Nov.–Dec. 1997. doi:10.2514/2.4176.
- M. Kelly. An Introduction to Trajectory Optimization: How to Do Your Own Direct Collocation. *SIAM Review*, 59(4):849–904, 2017. doi:10.1137/16M1062569.
- P. Lu. Introducing Computational Guidance and Control. *Journal of Guidance, Control, and Dynamics*, 40(2):193–193, 2017. doi:10.2514/1.G002745.
- Y.i Mao, D. Dueri, M. Szmuk, and B. Açıkmeşe. Successive Convexification of Non-Convex Optimal Control Problems with State Constraints. *IFAC-PapersOnLine*, 50(1):4063–4069, 2017. ISSN 2405-8963. doi:10.1016/j.ifacol.2017.08.789. 20th IFAC World Congress.
- A. C. Morelli, C. Hofmann, and F. Topputo. Robust Low-Thrust Trajectory Optimization Using Convex Programming and a Homotopic Approach. *IEEE Transactions on Aerospace and Electronic Systems*, 58(3):2103–2116, 2022. doi:10.1109/TAES.2021.3128869.
- A. H. Nayfeh. *Perturbation Methods*. Wiley, Weinheim, 2000. doi:10.1002/9783527617609.
- K. Oguri. Successive Convexification with Feasibility Guarantee via Augmented Lagrangian for Non-Convex Optimal Control Problems. In *2023 62nd IEEE Conference on Decision and Control (CDC)*, pages 3296–3302, December 2023. doi:10.1109/CDC49753.2023.10383462.
- K. Oguri and J. W. McMahon. Robust Spacecraft Guidance Around Small Bodies Under Uncertainty: Stochastic Optimal Control Approach. *Journal of Guidance, Control, and Dynamics*, 44(7):1295–1313, 2021. doi:10.2514/1.G005426.
- R. S. Park and D. J. Scheeres. Nonlinear Mapping of Gaussian Statistics: Theory and Applications to Spacecraft Trajectory Design. *Journal of Guidance, Control, and Dynamics*, 29(6):1367–1375, 2006. doi:10.2514/1.20177.
- M. Schaller, G. Banjac, S. Diamond, A. Agrawal, B. Stellato, and S. Boyd. Embedded Code Generation With CVXPY. *IEEE Control Systems Letters*, 6:2653–2658, 2022. doi:10.1109/LCSYS.2022.3173209.
- H. Schaub and J. L. Junkins. *Analytical Mechanics of Space Systems*. AIAA Education Series, Reston, VA, 4th edition, 2018. doi:10.2514/4.105210.
- J. A. Starek, B. Açıkmeşe, I. A. Nesnas, and M. Pavone. *Spacecraft Autonomy Challenges for Next-Generation Space Missions*, pages 1–48. Springer Berlin Heidelberg, Berlin, Heidelberg, 2016. ISBN 978-3-662-47694-9. doi:10.1007/978-3-662-47694-9_1.

- M. Valli, R. Armellin, P. Di Lizia, and M. R. Lavagna. Nonlinear Mapping of Uncertainties in Celestial Mechanics. *Journal of Guidance, Control, and Dynamics*, 36(1):48–63, 2013. doi:10.2514/1.58068.
- Z. Wang and M. J. Grant. Minimum-fuel low-thrust transfers for spacecraft: A convex approach. *IEEE Transactions on Aerospace and Electronic Systems*, 54(5):2274–2290, 2018. doi:10.1109/TAES.2018.2812558.
- M. Willis, K. T. Alfriend, and S. D’Amico. Second-order solution for relative motion on eccentric orbits in curvilinear coordinates. In *AAS/AIAA Astrodynamics Specialist Conference*, number AAS 19-810. American Astronautical Society, 2019a.
- M. Willis, T. A. Lovell, and S. D’Amico. Second-Order Analytical Solution for Relative Motion on Arbitrarily Eccentric Orbits. In *AAS/AIAA Spaceflight Mechanics Meeting*, number 19-364 in Advances in the Astronautical Sciences. Univelt, January 2019b.
- Wolfram Research, Inc. Mathematica, Version 13.3, 2023. URL <https://www.wolfram.com/mathematica>. Champaign, IL, 2024.

A Generating and Formatting the Mixed Monomials and the Non-linear Fundamental Solution Expansions

A.1 Computerized generation and manipulation of monomial representations

To implement our methodology, one needs a well-ordered and unambiguous way of constructing and manipulating monomial sequences. We use a positional power representation of monomials and we represent sequences of monomials in 2D arrays. The easiest way to explain this is with a full end-to-end example, but Giorgilli and Sansottera (2011) and Jorba (1999) give more context on similar techniques. Here we drop the initial condition notation “ $x_i(0)^j$ ” in favor of the more compact x_i^j . Consider a 3-state system with states x_1, x_2, x_3 . The array representation of the monomial $x_1^a x_2^b x_3^c$ for integer powers $a, b, c \geq 0$ is $[a, b, c]$. These are stacked row-wise to reproduce sequences of monomials as needed. For example, we represent $\mathbf{c}_1 = \mathbf{x} = (x_1, x_2, x_3)^\top$ as the following array:

$$\text{arr}(\mathbf{c}_1) = \begin{bmatrix} 1 & 0 & 0 \\ 0 & 1 & 0 \\ 0 & 0 & 1 \end{bmatrix} \quad (60)$$

The following functional code snippet constructs all rows of a desired $\text{arr}(\mathbf{c}_j)$ for a system with N states by initializing $\text{arr}(\mathbf{c}_1)$ and then, order-by-order, appending the array representation (itself row-by-row) for higher-order terms up to and including nonlinearity order j . We take the array representation of a prior order (“**base_block**”) and generate all unique monomial power permutations for a new order (“**newblock**”), then step to the next order with **base_block** \leftarrow **newblock**.

```
import numpy as np
Identity_N = np.identity(N, dtype='int')
Kj = compute_Kj(N, j)

# Create arr(c1):
c_vec_array = np.identity(N, dtype='int')

# Extend c_vec_array to create arr(cj):
base_block = c_vec_array[0:N,0:N] # Initialize
k_prev = base_block.shape[0] # No. rows of base_block
for idx0 in range(j-1): # This order
    for idx1 in range(N): # This state
        term_mult = Identity_N[idx1, :]
        for idx2 in range(k_prev): # Which row of base_block?
            new_row = base_block[idx2, :] + term_mult # Make candidate
```

```

if idx1 == 0 and idx2 == 0:
    newblock = new_row.astype('int') # Initialize block
else:
    if not (new_row.tolist() in newblock.tolist()):
        newblock = np.row_stack([newblock, new_row])
c_vec_array = np.row_stack([c_vec_array, newblock]) # New order done
base_block = newblock # Step
k_prev = base_block.shape[0]

```

As an example output, we provide explicitly the third-order array representation of \mathbf{c}_j for the case of $N = j = 3$ below, with sub-blocks of orders 1, 2, and 3 partitioned for clarity:

$$\text{arr}(\mathbf{c}_3) = \begin{array}{|c|} \hline 1 & 0 & 0 \\ 0 & 1 & 0 \\ 0 & 0 & 1 \\ \hline 2 & 0 & 0 \\ 1 & 1 & 0 \\ 1 & 0 & 1 \\ 0 & 2 & 0 \\ 0 & 1 & 1 \\ 0 & 0 & 2 \\ \hline 3 & 0 & 0 \\ 2 & 1 & 0 \\ 2 & 0 & 1 \\ 1 & 2 & 0 \\ 1 & 1 & 1 \\ 1 & 0 & 2 \\ 0 & 3 & 0 \\ 0 & 2 & 1 \\ 0 & 1 & 2 \\ 0 & 0 & 3 \\ \hline \end{array} \quad (61)$$

where e.g. the fourth row (first second-order component) is x_1^2 , the eighth row is x_2x_3 , and the eleventh is $x_1^2x_2$. Note that for nonlinearities of order q , it can be shown that the resultant sub-block will have the following number of terms:

$$\dim(\text{sub-block } q) = \binom{N+q-1}{q} \quad (62)$$

Adding up the number of rows of all sub-blocks to the max order j , we recover Eq. (4).

With a computerized array representation of \mathbf{c}_j , the column-wise arrangement of all fundamental solutions to make Ψ_j is also specified. We defer the reader to our code for any more details in that regard. We now briefly discuss how the Jacobians $C_j = \frac{\partial \mathbf{c}_j}{\partial \mathbf{c}_1}$ are computed in a computerized fashion leveraging the array representation of \mathbf{c}_j . This Jacobian should be of size $K_j \times N$ and will be composed completely of monomials and scalars. To compute the elements of this it's easy to differentiate a row of $\text{arr}(\mathbf{c}_j)$ with respect to a state by removing a one from the entry corresponding to the state being differentiated, and retaining the prior power as the new multiplying coefficient. For example, $\frac{\partial}{\partial x_3}(1 \times [1, 0, 2]) = 2 \times [1, 0, 1]$, and $\frac{\partial}{\partial x_3}(1 \times [1, 1, 0]) = 0 \times [\dots]$. In this manner derivatives on the monomials are reduced to simple array operations.

A.2 Computing the nonlinear fundamental solution expansion from STTs

This is the first of three admissible methods for constructing $\Psi_j(t)$. Park and Scheeres (2006) introduces the state transition tensors (STTs) as a generalization of the more familiar state transition matrix. They

map initial deviations of a system to deviations at some time t , and are characterized by the scalar expansions below, borrowing their notation:

$$\delta x_i(t) = \sum_{p=1}^m \frac{1}{p!} \Phi_{i,k_1 \dots k_p} \delta x_{k_1}^0 \dots \delta x_{k_p}^0, \quad i = 1 : N \quad (63a)$$

$$\delta \dot{x}_i(t) = \sum_{p=1}^m \frac{1}{p!} f_{i,k_1 \dots k_p}^* \delta x_{k_1}^0 \dots \delta x_{k_p}^0 \quad (63b)$$

$$\delta \dot{x}_i(t) = \sum_{p=1}^m \frac{1}{p!} \dot{\Phi}_{i,k_1 \dots k_p} \delta x_{k_1}^0 \dots \delta x_{k_p}^0 \quad (63c)$$

where summation convention is used, with $k_j \in \{1, \dots, N\}$, and subscripts k_j denote the k_j^{th} component of the state vector:

$$\Phi_{i,k_1 \dots k_p} = \frac{\partial^p x_i}{\partial x_{k_1}^0 \dots \partial x_{k_p}^0} \quad (64)$$

$$f_{i,k_1 \dots k_p}^* = \left. \frac{\partial^p f_i}{\partial x_{k_1}^0 \dots \partial x_{k_p}^0} \right|_* \quad (65)$$

The STTs have their own unique order-dependent dynamics. Park and Scheeres (2006) presents the dynamics for the STTs again element-by-element, up to fourth order. We compute them this way, getting the necessary Jacobian terms of Eq. (65) (necessary for STT numerical integration) via automatic differentiation.

This STT representation is fundamentally redundant, e.g. the 3rd-order STT components associated with $\delta x_1^0 \delta x_2^0 \delta x_1^0$, $\delta x_1^0 \delta x_1^0 \delta x_2^0$, $\delta x_2^0 \delta x_1^0 \delta x_1^0 \dots$ are all equal yet appear individually within the STT structure. We can compute a fundamental solution from its associated STT terms as below:

$$\psi_{i, \mathcal{O}(x^q)} = \frac{\mathcal{R}}{q!} \Phi_{i,k_1 \dots k_q} \quad (66)$$

where $i=1:N$ denotes the i^{th} component (row) of the fundamental solution, $\mathcal{O}(x^q)$ denotes some particular column of Ψ_j associated with the order- q STT component of interest, and \mathcal{R} is the number of repeats of the relevant STT term – for example, for $N = 2$, $j = 2$, and $\psi_{i, x_1 x_2}$, we compute $\mathcal{R} = 2$ because we have two repeated STTs, $\Phi_{i,1 \cdot 2} = \Phi_{i,2 \cdot 1}$. Lastly recall that the ordering of the columns of Ψ_j corresponds to the ordering of the corresponding monomials in \mathbf{c}_j .

A.3 Computing the nonlinear fundamental solution expansions analytically

Now we discuss a second method for constructing $\Psi_j(t)$. The spacecraft relative motion problem, our example in this work, is extremely well-studied in literature due to its historical significance and enduring importance in spaceflight. For this problem there has been an enormous amount of past work to develop completely analytic nonlinear approximations of the solution of the satellite relative motion equations. These can be adopted directly to replace the numerically computed nonlinear functions used in this work. Here we provide a brief discussion about how such solutions can be derived. These “solutions” approximate, via low-order series expansion in the initial states, the true behavior of the nonlinear differential equations of spacecraft relative motion given by Casotto (2016). Typically these are obtained by perturbation methods (Nayfeh, 2000; Hinch, 1991), most typically a straightforward expansion. Here we preview such a methodology briefly with a shortened discussion of how the second-order analytic STTs are derived (Butcher et al., 2016). In general, the state can be expanded in a perturbation series:

$$\mathbf{x}(\tau) = \mathbf{x}_1(\tau) + \varepsilon \mathbf{x}_2(\tau) + \varepsilon^2 \mathbf{x}_3(\tau) + \dots \quad (67)$$

where ε is a small parameter, $\tau = nt$, and typically the states are rendered in a non-dimensional form. The function $\mathbf{x}_1(\tau)$ is the solution to the unperturbed linearized (CW) dynamics, and the subsequent functions correct for nonlinearities in the dynamics, and possibly also target orbit eccentricity.

First, the dimensionless CW equations are solved to obtain $\mathbf{x}_1(\tau)$. Then, we perform a nonlinear expansion of the nonlinear equations of relative motion (see e.g. Schaub and Junkins (2018) for Keplerian or Casotto (2016) for non-Keplerian) up to a desired order in the states, then substitute the expansion of Eq. (67) into the dynamics. The dynamics are then parsed order-by-order starting with the unperturbed linear problem $\mathcal{O}(\varepsilon^0)$ and continuing to all other powers of ε . From the $\mathcal{O}(\varepsilon^1)$ part, the model equations are rearranged into a form below separating all perturbations up to second-order in the states (constituting F_2) from the dimensionless Clohessy-Wiltshire (CW) ODE equations:

$$\begin{pmatrix} x_2'' - 2y_2' - 3x_2 \\ y_2'' + 2x_2' \\ z_2'' + z_2 \end{pmatrix} = F_2(\tau, x_1, y_1, z_1, x_1', y_1', z_1') \quad (68)$$

The solutions to these equations can be found using symbolic software to evaluate the following inverse Laplace transform:

$$\begin{pmatrix} x_2(\tau) \\ y_2(\tau) \\ z_2(\tau) \end{pmatrix} = \mathcal{L}^{-1} \left(\begin{bmatrix} s^2 - 3 & -2s & 0 \\ 2s & s^2 & 0 \\ 0 & 0 & s^2 + 1 \end{bmatrix}^{-1} \mathcal{L}(F_2(\tau)) \right) \quad (69)$$

The inverted matrix is the transfer matrix of the CW system, and $F_2(\tau)$ is obtained by substituting the normalized CW solution into all states in the right side of Eq. (68). The velocity states $x_2'(\tau)$, $y_2'(\tau)$, $z_2'(\tau)$ are then obtained by simple symbolic differentiation of the solutions above.

For the analytic version of the third-order nonlinear solutions that we numerically computed to build Ψ_j , in local Cartesian coordinates, consult Butcher et al. (2016). Note their solution is trigonometrically sorted for compactness instead of in terms of the monomials. Butcher et al. (2017) explores a similar approach in both Cartesian coordinates and curvilinear coordinates, which offer greater accuracy because they better accommodate the natural curvature of the orbit geometry. These solutions also apply corrections for nonzero target orbit eccentricity, which improves their fidelity in a true flight setting. Note that the eccentricity-linear part of the curvilinear solutions are derived from an equation which contains an error, which is addressed in the Appendix of Willis et al. (2019a). That work also derives its own curvilinear solutions and provides a nice discussion of other analytic solutions in literature for this problem. Note that for long-duration problems, it becomes necessary to account for non-Keplerian perturbations such as J_2 (Burnett et al., 2018). The problem of deriving nonlinear analytic solutions to this problem presents a higher degree of difficulty than the Keplerian case. The appealing possibilities in use of these solutions in guidance applications (particularly if they're analytic and time-explicit), as demonstrated by this paper, might breathe new life into the academic efforts for their derivation.

A.4 Computations using Differential Algebra

It's well-known that the STTs and Differential Algebra (DA) can be used to provide the same information about the nonlinear expansions in the vicinity of a reference. Thus DA constitutes a third method for building $\Psi_j(t)$. Indeed, we have tested this, computing Ψ_j using Pyaudi (Izzo et al., 2022), which offers speed advantages over the STTs. Similarly to the case of using STTs to build Ψ_j , in general $\Psi_j(t)$ can be constructed for discrete times $t_i \in [t_0, t_1, \dots, t_f]$ by computing the higher-order Taylor map (HOTM) from t_0 to t_1 , then t_0 to t_2 , etc. for all times $t_i > t_0$, extracting the coefficients for every time, and ordering them appropriately to build a corresponding $\Psi_j(t_i) \forall t_i$. Here we contextualize some of our work within the DA framework as outlined in Berz (1999). For this discussion we borrow and synthesize Berz' notation where needed. We defer the unfamiliar reader to their thorough introduction to DA so as not to risk the confusion from a compressed summary.

First we note that our K_j -dimensional space $\mathcal{C}^{(N)}$ (facilitated by the j^{th} -order nonlinear expansion) is directly related to the vector space ${}_jD_N$. In particular, let $d_k = [x_k]$ denote the higher-order differential structure induced by a j^{th} -order expansion of the k^{th} element of coordinates $\mathbf{x} \in \mathbb{R}^N$. Then the Taylor expansion T_f of some function f can be expanded into the vector space ${}_jD_N$:

$$[f] = [T_f] = \sum_{q_1 + \dots + q_N \leq j} \alpha_{q_1, \dots, q_N} \cdot d_1^{q_1} \dots d_N^{q_N} \quad (70)$$

Berz computes, via consideration of the tuples q_1, \dots, q_N , that the dimensionality of ${}_jD_N$ is as follows:

$$\dim({}_jD_N) = \binom{N+j}{N} \quad (71)$$

We observe the following similarity, where $\mathcal{C}^{(N)} \subseteq \mathbb{R}^{K_j}$, and K_j is given by our Eq. (4):

$$\dim({}_jD_N) = K_j + 1 \quad (72)$$

The difference here is that ${}_jD_N$ contains the “Real” component (the reference point about which the nonlinear expansion occurs) by definition, but $\mathcal{C}^{(N)}$ does not, because in general our parameterization works specifically with state deviations from a reference.